



Surface thermodynamics and radiative budget in the Sahelian Gourma: Seasonal and diurnal cycles

Françoise Guichard^{a,*}, Laurent Kergoat^b, Eric Mougin^b, Frank Timouk^b, Frédéric Baup^b, Pierre Hiernaux^b, François Lavenu^b

^a CRNM/GAME, URA 1357 (CNRS and Météo-France), 42 Avenue Coriolis, 31057 Toulouse Cedex, France

^b CESBIO, UMR 5126 (CNES/CNRS/IRD/UPS), 18 Avenue Edouard Belin, bpi 2801, 31401 Toulouse Cedex 9, France

ARTICLE INFO

Keywords:

Sahel
Monsoon
Surface
Radiative flux
Longwave
Shortwave

SUMMARY

Our understanding of the role of surface–atmosphere interactions in the West African monsoon has been particularly limited by the scarcity of measurements. The present study provides a quantitative analysis of the very pronounced seasonal and diurnal cycles of surface thermodynamics and radiative fluxes in the Central Sahel. It makes use of data collected from 2002 to 2007 in the Malian Gourma, close to Agoufou, at 1.5°W–15.3°N and sounding data collected during the AMMA field campaign.

The seasonal cycle is characterized by a broad maximum of temperature in May, following the first minimum of the solar zenith angle (SZA) by a few weeks, when Agoufou lies within the West African Heat Low, and a late summer maximum of equivalent potential temperature (θ_e) within the core of the monsoon season, around the second yearly maximum of SZA.

Distinct temperature and moisture seasonal and diurnal dynamics lead to a sharpening of the early (late) monsoon increase (decrease), more steadiness of θ_e and larger changes of relative humidity in between. Rainfall starts after the establishment of the monsoon flow, once temperature already started to decrease slowly, typically during June. Specific humidity increases progressively from May until August, while the monsoon flow weakens during the same period.

Surface net radiation (R^{net}) increases from around 10-day mean values of 20 W m⁻² in Winter to 120–160 W m⁻² in late Summer. The increase is sharper during the monsoon than before, and the decrease fast. The seasonal cycle of R^{net} arises from distinct shortwave and longwave fluctuations that are both strongly shaped by modifications of surface properties related to rainfall events and vegetation phenology (with a decrease of both surface longwave emission and albedo). During the monsoon, clouds and aerosols reduce the incoming solar radiation by 20–25% (about 70 W m⁻²). They also significantly enhance the day-to-day variability of R^{net} . Nevertheless, the surface incoming longwave radiative flux (LW^{in}) is observed to decrease from June to September. As higher cloud covers and larger precipitable water amounts are typically expected to enhance LW^{in} , this feature points to the significance of changes in atmospheric temperature and aerosols during the monsoon season.

The strong dynamics associated with the transition from a drier hot Spring to a brief cooler moist tropical Summer climate involves large transformations of the diurnal cycle, even within the monsoon season, which significantly affect both thermodynamical, dynamical and radiative fields (and low-level dynamics). In particular, for all moist Summer months except August, specific humidity decreases in such a way during daytime that it prevents an afternoon increase of θ_e .

In agreement with some previous studies, strong links are found between moisture and LW^{net} all year long and a positive correlation is identified between R^{net} and θ_e during the monsoon.

The observational results presented in this study further provide valuable ground truth for assessing models over an area displaying a rich variety of surface–atmosphere regimes.

© 2008 Elsevier B.V. All rights reserved.

Introduction

Energy and water fluxes at the land–atmosphere interface are recognized as important actors of the West African monsoon (WAM). They play a crucial role in the mechanisms that have been put forward to explain several WAM specific features (Nicholson,

* Corresponding author. Tel.: +33 5 61 07 96 72.

E-mail address: francoise.guichard@meteo.fr (F. Guichard).

2000), for scales ranging from regional and interannual (Charney, 1975; Eltahir and Gong, 1996), seasonal (Ramel et al., 2006) down to mesoscale ones (Taylor and Lebel, 1998).

As an example, the sensitivity of the WAM to surface albedo has been, and still is, the object of a number of studies, focused on a variety of space and time scales. This line of investigation can be traced back to the mechanism hypothesized by Charney (1975) in an attempt to find causes for the dramatic multi-decadal regional drought that started at the end of the 1960's and was particularly severe in the 1970's and 1960's over West Africa. As reviewed by Nicholson (2000) however, a number of subsequent observational studies led to a modification of the too simple perception prevailing in the 1970–80's regarding the nature and extend of land surface changes. In particular, they showed that the variability of the land surface could not be simply attributed to human-induced changes, but involved more complex modes of soil-surface-vegetation-atmosphere interactions and climatic variability. This further shed doubts about the dominant role attributed to land use change by some previous modelling works in order to explain the persistence of the drought. The evolution of ideas summarized above also points to the value of observations in guiding modelling and theoretical approaches in a fruitful way.

A number of modelling studies focused on the role of land-atmosphere interactions on the WAM have relied on drastic assumptions regarding the treatment of land surface properties. Their purpose was more towards identifying the likeliness and characterizing the functioning of specific mechanisms, for instance the impact of soil moisture-radiation coupling (Eltahir, 1998) or the role of the vegetation dynamics (Xue, 1997). While such an academic approach is quite adapted to its goal, it cannot aim at explaining observations in a quantitative way (Zheng and Eltahir, 1998). In fact, the mechanisms involving couplings between parameterised processes, such as radiative, surface, vegetation, boundary layer, convection and cloud processes, are difficult to reproduce with surface-atmosphere coupled models. Their proper treatment also relies on an adequate coherency of the levels of development and sophistication of each parameterised process. Currently the wide diversity of treatments found in existing models is likely a major cause for the large range of sensitivities found among climate models (Dirmeyer et al., 2007).

In a broad sense, land surface properties play a role in the mechanisms of interaction actually taking place between the atmosphere and the underlying surface. Therefore, it is essential for a model to accurately depict such properties, together with the associated surface fluxes. In that way, the chain of interacting processes (and resulting mechanisms) arising in the model is more likely to correspond to those observed. In this respect, observational datasets provide valuable information. In the past decades, several datasets have been collected over continent with ground based instruments (ARM¹, LBA², FIFE³ among others); they led to an improvement of models and new approaches of model evaluation (e.g.; Betts, 2004). In the Sahel, where routine observations are sparse, field experiments documenting land surface properties and fluxes have not been very numerous either. An important step in our knowledge was acquired from the data collected during the HAPEX-Sahel experiment (Goutorbe et al., 1994), 15 years ago. It was however limited in space and time as it took place in Niger, close to Niamey, from August to October 1992, thus mostly documenting the last half of a monsoon season and the dry-down period. Two key distinctive characteristics of the Sahel area are however, (i) the existence of sharp climatological latitudinal gradients of rainfall, vegeta-

tion cover, albedo, and (ii) the high interannual variability of the monsoon season. This was indeed at the core of the motivation that led to the development of the recent AMMA project (Redelsperger et al., 2006).

Over West Africa, surface net radiation (R^{net}) and low-level equivalent potential temperature (θ_e) are important actors of the WAM. Indeed, values and variations of these variables are central to existing hypotheses and theories of the WAM monsoon, whether they agree or not, for instance considering the contrasting views of Charney (1975) and Eltahir and Gong (1996). The first one stresses the significance of the Sahelian surface albedo and energy budget while the second emphasizes the control of the latitudinal gradients of θ_e from the Gulf of Guinea to the Sahelian zone on the strength of the monsoon flow.

R^{net} is directly related to the magnitude of surface-atmosphere heat exchanges, which strongly control boundary layer and low-level dynamics. Low-level θ_e is a key parameter regarding moist convection. Across West Africa, it mirrors the changes in magnitude of convective available potential energy (CAPE) (Guichard et al., 2008), an index traditionally thought of as a good indicator of the strength of deep precipitating convection whether, when and where it occurs. It can also reflect the existence of convection inhibiting factors leading to the build-up of high low-level θ_e , and therefore CAPE (e.g. Redelsperger et al., 2002). Analysing these two parameters and how they relate to each other at different scales is an important issue. In this study, we use meteorological and radiative data collected in Central Sahel, within the Malian Gourma, to address this issue at a local spatial scale. It is based on a quantitative analysis of surface thermodynamics and radiative budget derived from a multi-year dataset over an area that has not been documented so far. This allows assessing the relevance of mechanisms of land surface-atmosphere feedbacks, and how they relate to those emerging from previous studies focused on other geographical areas (e.g.; Betts and Ball, 1998; Small and Kurc, 2003).

This dataset is presented in next section. In this paper, we focus on the seasonal cycle, including seasonal variations of the diurnal cycle. Major features of these cycles are presented regarding meteorological fields and radiative fluxes in the two following sections. From there, synthetic diagnostics characterizing and relating radiative and thermodynamic fields during the monsoon season are discussed.

Data and method

The measurement site is located in the central part of the Sahel, at 15°20'40"N and 1°28'45"W in the Malian Gourma. It is referred to as Agoufou, from the name of the close by village. Instruments are deployed in grassland, over sandy soil, which is the dominant surface type in the Gourma area, with an occupation rate of around 65%. The 35% remnants correspond to bare rocky or very shallow loamy soils (28%) and loamy-clay soils found in depressions (approximately 7%).

An automatic weather station (AWS), installed in Agoufou, has been acquiring data at a 15-min time step since April 2002. The four components of the radiation balance are measured with a CNR1 (Kipp and Zonen). The site is homogeneous over several kilometres, thus allowing a good estimation of the reflected solar and emitted radiation in addition to incoming radiative fluxes (Samain et al., 2008). Air temperature and humidity are recorded with a HMP45C (Vaisala) together with wind speed and direction (A100R and W200P, Vector), and rainfall (Cimel pluviograph) at 2 m above ground level (AGL). Data are stored in a datalogger (CR10X, Campbell).

Due to environment harshness and site remoteness, the dataset presents some gaps, which most often take the form of multi-day

¹ ARM: atmospheric radiation measurement.

² LBA: Large-Scale Biosphere-Atmosphere Experiment in the Amazonia.

³ FIFE: First ISLSCP (International Satellite Land Surface Climatology Project) Field Experiment.

intervals. Daily average values have been computed only when there was no hole in the corresponding 24-h period, the same rule was followed for computing running means, daily minima and maxima as well as diurnal composites; in practice, this is not a very limiting constraint given the actual structure of gaps.

Surface pressure (P_s) is recorded since 2006 only. However, seasonal variations of P_s are relatively small. The larger fluctuations occur between late December and Spring, when P_s drops from about 982 hPa down to 972 hPa, at times when Agoufou is located within the Heat Low, semi-diurnal tides also account for a 2 to 4 hPa range of fluctuations. P_s is used for computing θ_e and the pressure difference between the lifting condensation level (lcl) pressure and the surface ($P_s - Plcl$). As these variables are not very sensitive to the observed range of fluctuations, a constant P_s of 975 hPa has been used for calculations presented below.

A simple estimation of cloud shortwave radiative forcing at the surface has been carried out from the AWS data. It consists in computing for day D and each 15-min interval I of this day the maximum incoming SW radiative flux recorded within the $N = 2P + 1$ days centred on day D (criterion C_1). This provides a crude estimate of clear sky incoming shortwave flux, $SW_{CS_1}^{\text{in}}$. In practice, N was varied from 10 to 30. An additional criterion (C_2) was tested in order to weaken the impact of unwanted local spikes that can occur under partly cloudy conditions. To do so, a procedure similar to the one presented above is applied to $SW_{CS_1}^{\text{in}}$, except computing now the minimum instead of the maximum. With $N = 30$, ($C_1 + C_2$) essentially provides the same monthly estimate as the one obtained with (C_1) alone for $N = 10$. The most obvious drawback of such simple methods arises under persistently and heavily aerosol-loaded skies. In Agoufou, such conditions are typically the more frequent from mid-May to mid-July. In that case, (C_1) clear sky estimates are more representative of the less aerosol-loaded day of the N -day period considered as assessed by visualization of time series.

Some additional inferences between surface measurements and the atmosphere above are obtained, either directly from sunphotometer data, or more indirectly from the ECMWF analysis and from high-resolution sounding data.

The sunphotometer was installed in October 2002, within a few tens of metres from the AWS. It provides estimations of aerosol optical thickness (AOT) and precipitable water vapour content (PWV) during daytime under cloud-free conditions⁴. Each day, all PWV estimates available from 10Z to 16Z have been averaged to provide “daily-mean” values.

The ECMWF analysis of the closest atmospheric column is used. It consists of 6-h sampled vertical profiles whose stretched vertical resolution ranges from less than 100 m in the lowest levels to about 550 m at 5 km AGL. (In 2003, the horizontal resolution of the analysis was about 40 km.)

Sounding data provide a more reliable depiction of the atmosphere, especially in the low levels. Thus, sounding data from Niamey have been chosen because Niamey constitutes the closest location where sounding data are available with an appropriate time sampling (6-h) over the whole year 2006 (Parker et al., 2008; Nuret et al., 2008). They have been interpolated on a common vertical grid whose resolution ranges from 10 to a few tens of meters.

Seasonal cycle of meteorological data: thermodynamics and wind

Major features of the seasonal cycle are presented below and in next section for year 2003. Except when otherwise stated, broad features discussed below are valid for the other years as well, be-

yond interannual variability. In particular, the course of each of these years is well-defined by the succession of periods indicated in Fig. 1. As typical of areas affected by monsoons, the seasonal cycle is characterized by a strong variability of atmospheric parameters. It is traditionally described as being composed of three distinct periods in the Gourma: the cold season, the hot season and the monsoon, and the three transition periods in between (Ag Mahmoud, 1992). Thus, the cold season roughly corresponds to the successive cooling and dry warming phases (November to February) and the hot season to the hot, moist springtime (April to mid-June) of Fig. 1.

The establishment of the monsoon

The monsoon season is well delineated from the sequence of summer rainfall events (Fig. 1). Outside of June to September, rainfall events are unusual. In 2003, the rainfall amount was above the average for the Sahel as a whole (Agrhymet Bulletin, 2003); it was the case at the Agoufou site as well. Rainfall events were numerous, and regular in time, i.e. no dry spell occurred.

The first significant monsoon rainfall occurred on day of year 168 in 2003, about five weeks after the monsoon became steadily established, on day 134 (Fig. 1). More generally, for the years considered, the first notable rainfall event typically occurs a few days to a few weeks after the establishment of a sustained low-level monsoon flow, once the inter-tropical discontinuity (ITD) has definitely migrated northwards for the Summer (Fig. 2a and b) and the 2m-temperature (T_{2m}) started to decrease. Low-level wind reversals between Harmattan and monsoon flows can start as early as April however. They reflect that Agoufou is then often located alternately on either side of the inter-tropical discontinuity (ITD), when the ITD is sharp and well-defined, or within it. During this April–May transitional phase, time series of both 2m-specific humidity, q_{2m} (Fig. 1) and precipitable water vapour, PWV (Fig. 3) consistently display series of peaks and jumps.⁵ Several of them are very likely local manifestations of pulsations of the monsoon flow occurring at larger spatial scales, as implied by the frequent occurrence of variations similar to those observed at Agoufou at remote sites such as Bamba, Gao or Tombouctou (not shown).

The specific humidity jump in May also coincides with the start of a sustained 2m relative humidity (RH_{2m}) increase (Fig. 4). The distinct evolution of RH_{2m} and q_{2m} reflects the high values of T_{2m} that are still prevailing from mid-May to mid-June (days of year 140–165). In fact, in the absence of any significant rainfall, daily-mean soil temperature at 5 cm remains above 40 °C except for one day. At the same time, T_{2m} decreases weakly, which likely reflects that advection of cooler (and moister) air slightly dominates T_{2m} variations. This slow T_{2m} decrease is interrupted by the sharp drop occurring with the first significant rainfall event (day of year 168 in Fig. 1).

At the same time, the 2m wind speed increases steadily, from early May until June when it reaches its year-maximum (Fig. 2c). Later on, it decreases in July and then again in August. Most isolated spikes are linked to convective bursts, as can be guessed from the coincidence of many of them with the timing of rainfall per event. This Spring to late Summer evolution is qualitatively similar to the ECMWF analysis of 10-m wind speed and is associated with a weakening of the monsoon flow, in terms of both low-level strength and depth (Fig. 2a and b). Such a trend along the monsoon season actually occurs further South in Niamey at 13.2°N (Lothon et al., 2008). In Agoufou, this feature may involve a decreasing

⁴ The aeronet cloud screened data are used, this correspond to “level 15” type of data.

⁵ Strong links are indeed found between q_{2m} and PWV, down to synoptic scales, especially outside of the summer months, when both q_{2m} and PWV fluctuations are larger, and beyond the fact that these two fields exhibit distinct diurnal and seasonal dynamics (Bock et al., 2008).

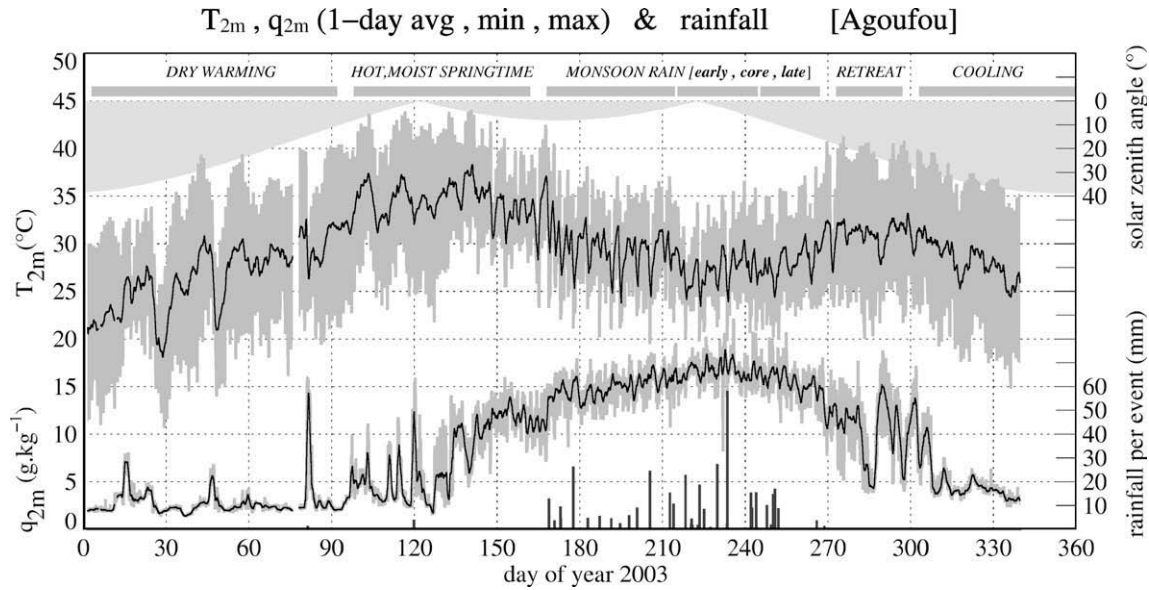


Figure 1. Time series of 2m temperature T_{2m} (upper curve) and specific humidity q_{2m} (lower curve) in 2003 (the black lines correspond to a 24-h running mean and the dark grey shadings delineate 24-h minimum and maximum values), rainfall amounts per rainy event (bottom bars) and midday solar zenith angle (light shading). – different time periods are roughly delimited by the top thick grey lines with their name given above.

influence of the Heat Low, once the latter migrates farther to the North–West. This hypothesis is consistent with the increase of the Westerly wind component from May to the end of July. In any case, it implies a weakening of the significance of horizontal advection within the core of the monsoon.

Temperature and specific humidity

Considering now the whole year sequence, the seasonal variations of T_{2m} and q_{2m} are distinct. T_{2m} displays two maxima, one before and one after the – cool – monsoon (*monsoon rain* time period of Fig. 1), in May (within the *hot, moist springtime*) and October (*retreat*). The first T_{2m} maximum is the strongest (with a May monthly mean T_{2m} of about 35 °C). It signs the end of a warming started in late December–early January from the coldest of the year (*dry warming* sequence of Fig. 1). This warming coincides with the seasonal decrease of the minimum solar zenith angle from about 40° in late December down to 0° in early May.

The high value of temperatures prevailing from late April to late May (about 34–36 °C) together with the relatively weak positive warming of about 2 °C⁶ taking place within these few tens of days occur each year with a remarkable consistency from one year to the other at weekly time scale (not shown). Such a feature is not a-priori warranted in view of the high interannual variability of atmospheric dynamics typical of this time of year (transition between the dry season and the well established monsoon flow regime), also reflected in the large q_{2m} variations, even at the weekly scale. It implies that a mechanism involving turbulent, advective and radiative processes operates to damp the temperature increase within the Heat Low where Agoufou is laying.

The second T_{2m} maximum is weaker and its strength and timing vary more from one year to the other; it usually takes place in October, during the dry-down period following the monsoon (*retreat* in Fig. 1)⁷, and follows a short increase started in early September, about three weeks after the second minimum of the solar zenith

angle. Indeed, at that time of large incoming solar radiation (at the top of the atmosphere), the low levels are at their coldest of the Summer according to T_{2m} .

The seasonal cycle of q_{2m} is simpler with one single maximum; this maximum roughly coincides with the second minimum of the zenith angle. The atmosphere is essentially dry from November to the end of March (*dry warming*), apart from a few synoptic-scale events, and moist from May–June to September. However, q_{2m} , as PWV, still increases significantly and gradually until August, it decreases more sharply afterwards. Until day of year 210, rainfall events are well traced by sharp drops in T_{2m} minima (and jumps of RH_{2m} maxima) still fairly visible in 24-h mean values, but no such signature can be identified on q_{2m} here. During the phases of establishment of the monsoon flow (April–May) and retreat (September–October), q_{2m} variations are much stronger. As mentioned above, these phases display a particular sequence each year, this largely accounts for the strong interannual variability of q_{2m} observed here at local scale at those times of year.

Diurnal cycle

The grey shading in Fig. 1 highlights the significance of the diurnal T_{2m} range (DTR) along the year, and how it becomes perturbed and weaker once the atmosphere becomes moist, within the rainy period, but also prior to the onset of rainfall. On the other hand, the diurnal range of q_{2m} is the largest during the phases of establishment (Springtime) and retreat of the monsoon flow, but remains significant during most of the monsoon season. This is well captured by series of monthly mean diurnal cycles (Fig. 5). The diurnal cycle of q_{2m} varies significantly from May (morning peak) to August (flat cycle) to October (sharp afternoon drop). In July and September, q_{2m} is also characterized by an afternoon drop albeit less pronounced than in October, while in June, it displays both a well-defined morning maximum and an afternoon minimum. This marked seasonality involves variations of the sources and sinks of water vapour. In Spring, prior to rainfall, it is more directly linked to the diurnal dynamics of the monsoon flow as felt with the 2m wind than later in the season. For instance in May, the q_{2m} morning peak (at 9Z corresponding to 9 h local solar time LST, i.e. well after sunrise) matches the morning wind speed peak found all year long

⁶ This is indeed the time of year where the incoming solar radiative flux reaches its maximum at the top of the atmosphere.

⁷ The significance of this feature is typically “relatively” higher when the August cooling is stronger.

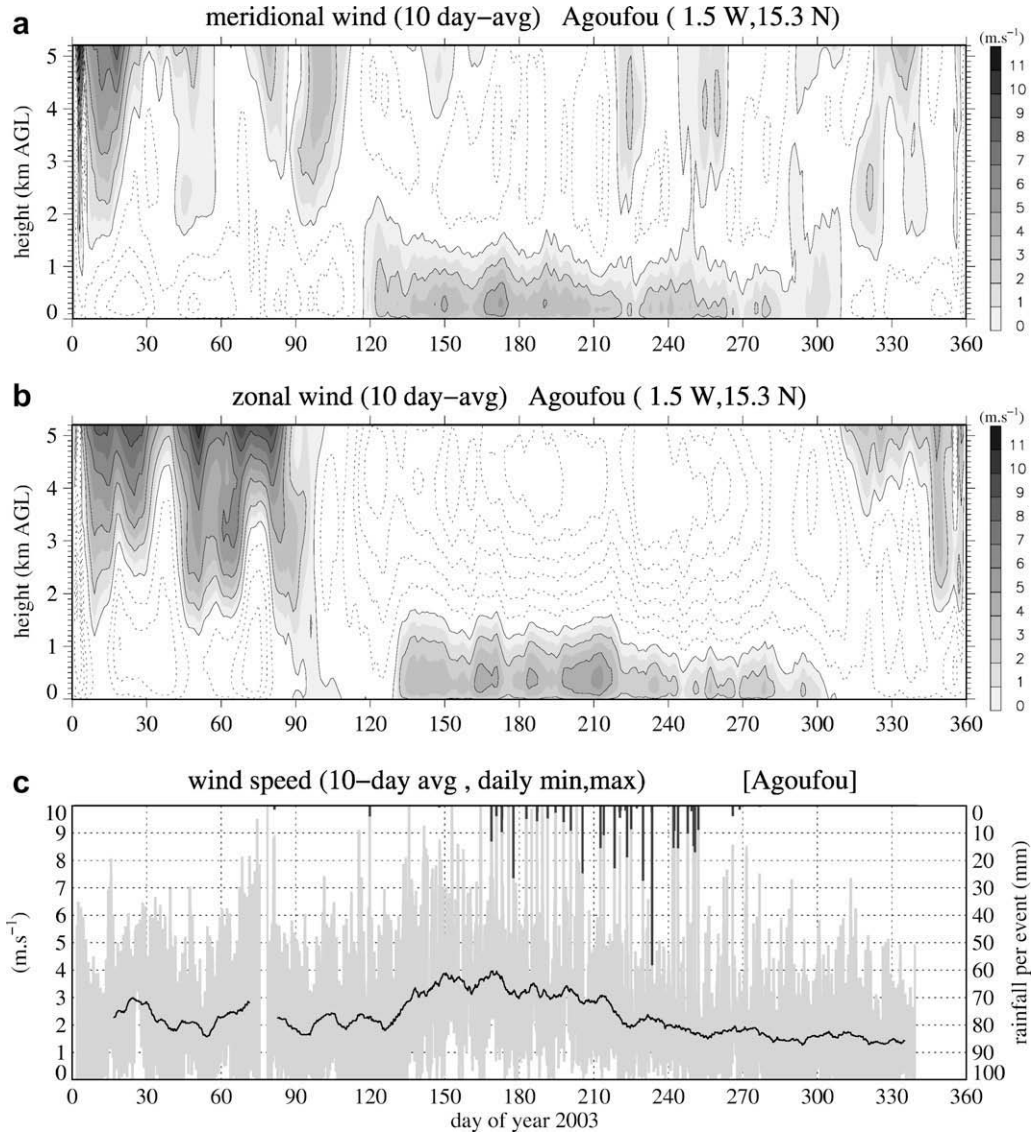


Figure 2. Time series of 10-day mean (a) meridional and (b) zonal wind and (c) wind speed at 2 m, in (a) and (b) the interval between isolines is 1 m s^{-1} with a grey colour scale for positive values (westerlies and southerlies); in (c) shading indicates 24-h minimum and maximum value.

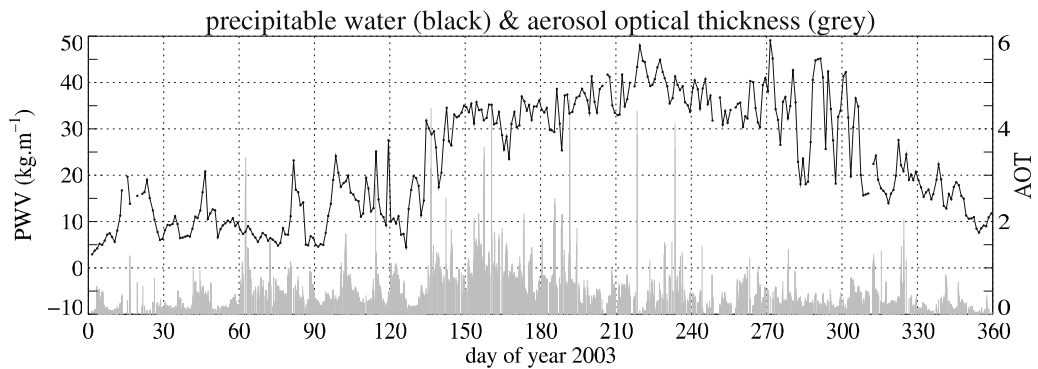


Figure 3. Time series of precipitable water PWV (average of daytime values, black line) and aerosol optical thickness AOT (at 1020 nm).

(Fig. 6) – it is well explained by daytime convective mixing of higher winds from low-level nocturnal jets (e.g.; Parker et al., 2005). The observed daytime drying can be explained by the growth of the daytime convective boundary layer (BL) within upper drier

air layers whose effect is not balanced by surface evapotranspiration nor any low-level moisture advection (Fig. 5). Sounding data of Niamey do show such large afternoon BL growths in June (not shown). As the season progresses from June to August, the

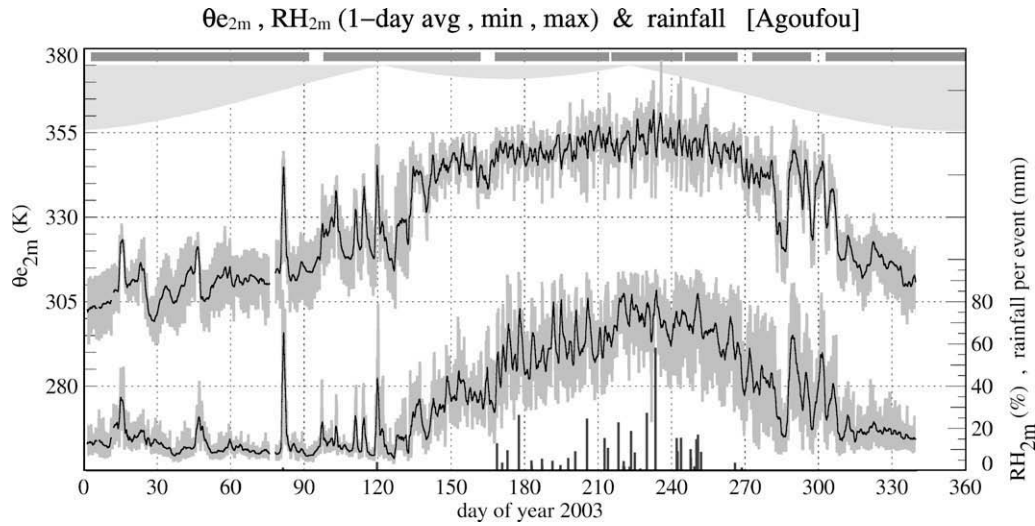


Figure 4. Same as Fig. 1 except for the 2m equivalent potential temperature $\theta_{e_{2m}}$ (upper curve) and relative humidity RH_{2m} (lower curve).

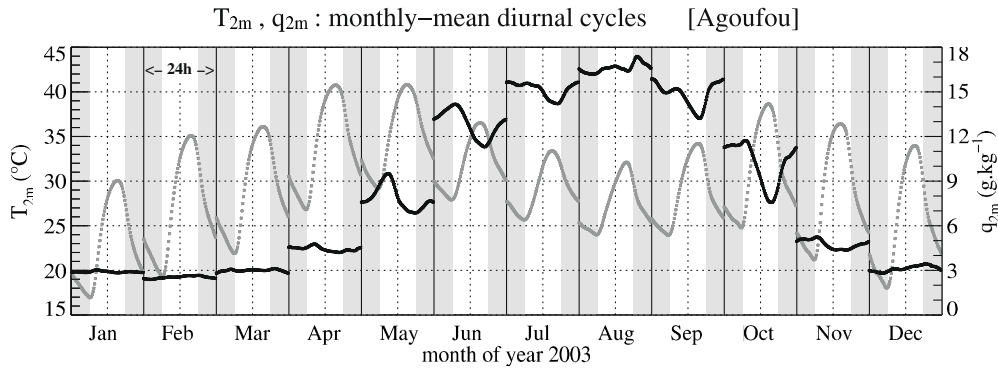


Figure 5. Time series of monthly mean diurnal cycle of 1-h average T_{2m} (grey dots) q_{2m} (black dots) – the alternate grey and white vertical bands correspond roughly to nighttime (18Z–0Z and 0Z–6Z) and daytime (6Z–18Z) hours.

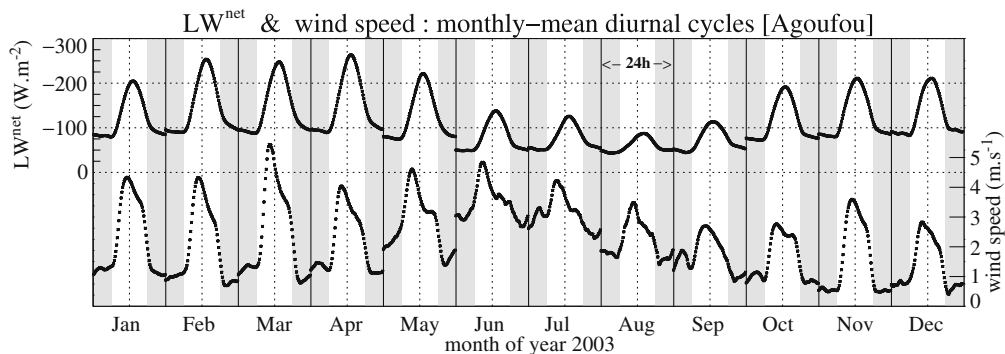


Figure 6. Same as Fig. 5 except for 1-h average LW^{net} (upper curve) and wind speed (lower curve).

flattening of the q_{2m} cycle is consistent with larger surface evapotranspiration, smaller surface heat fluxes (Timouk et al., 2009) and weaker daytime BL growths.

Fig. 6 also indicates that the enhancement of wind speed in June is mostly due to higher nighttime values, a feature still valid until September beyond the overall weakening of the wind speed along the monsoon season. This feature in turn involves a weakening of the LW radiative decoupling of the surface and overlying atmosphere as measured by DTR and LW^{net} . Indeed, from January to April, daytime winds are in the same range than in June, but the

strong surface cooling is associated with a quick damping of the 2m wind at sunset, and then, it appears to efficiently prevent the development of nighttime winds at the surface (the surface roughness length is not likely to change during that period, and thus cannot account for this functioning).

Equivalent potential temperature and relative humidity

In the introduction, we stressed the importance of the low-level equivalent potential temperature (θ_e) in existing schemes or

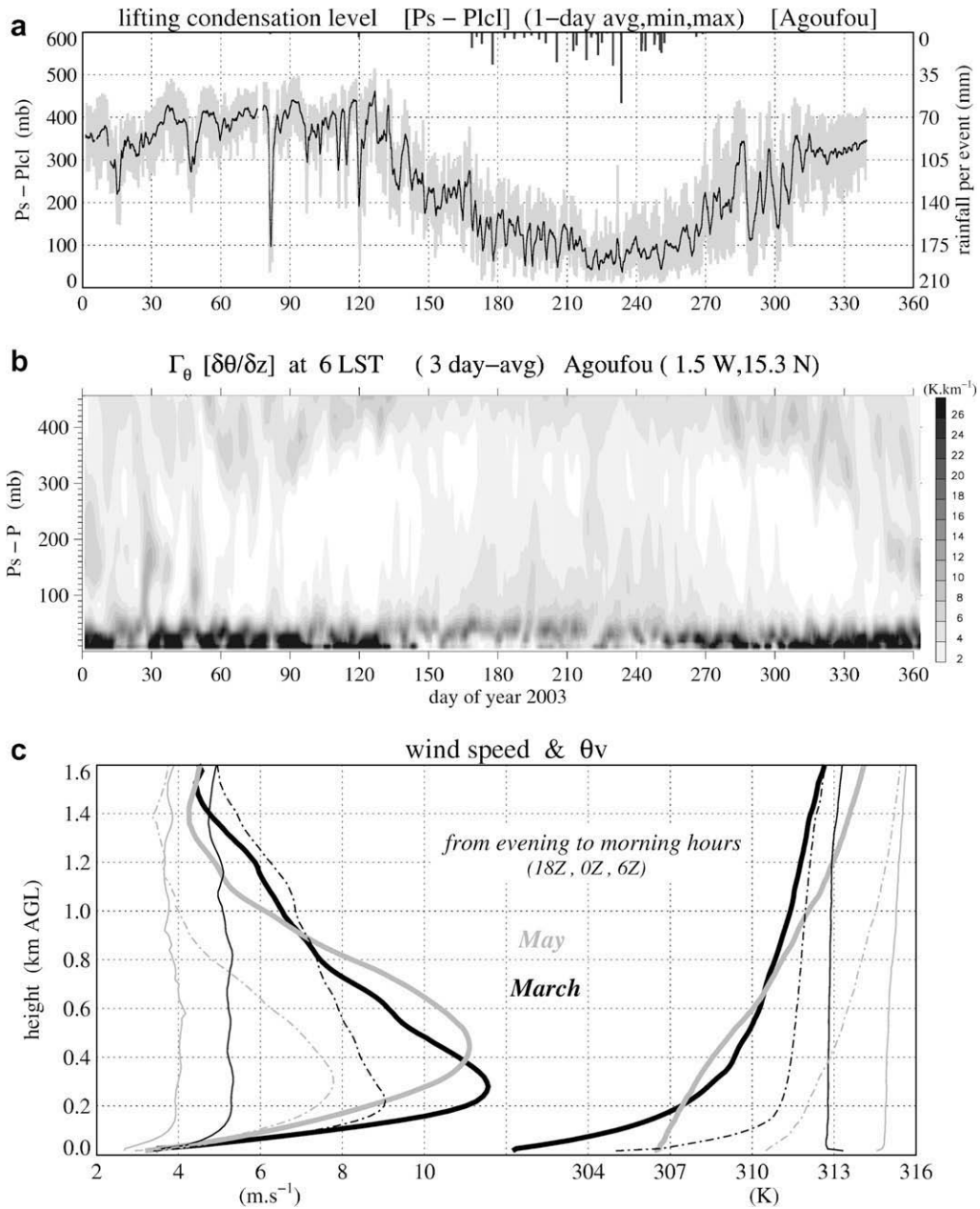


Figure 7. (a) Same as Fig. 1 except for the lifting condensation level (*lcl*) expressed as a departure from the surface pressure ($P_s - P_{lcl}$), (b) time-height series of lapse-rate $\delta\theta/\delta z$ at 6Z (3-day mean) and (c) March (black) and May (grey) monthly mean profiles of wind speed and virtual potential temperature θ_v , at Niamey (each curve is made from about 30 profiles). In (a) and (b) a value of $P_s - P_{lcl}$ of 100 mb (resp. 200, 300 and 400 mb) on the y-axis corresponds roughly to a height of 0.95 km AGL (resp. 2, 3.2 and 4.6 km AGL). P_s fluctuates around 975 mb by a few mb.

theories of the WAM. They emphasize either more local or larger scale mechanisms and controlling factors, but all involve consideration of moist convective processes (and most of the rain falling in the Gourma is of convective nature⁸). Fluctuations of 2m θ_e ($\theta_{e_{2m}}$) are controlled by T_{2m} and q_{2m} . In particular, their combined variations lead to sharpen $\theta_{e_{2m}}$ jumps and drops at the beginning and to a lesser extent at the end of the monsoon season (Fig. 4, upper curve). This damps somehow the fluctuations of $\theta_{e_{2m}}$ during the summer, which are weaker than if only controlled by the fluctuations of q_{2m} . Thus, T_{2m} and q_{2m} combine differently to produce high $\theta_{e_{2m}}$ within the core of the monsoon season in August (high q_{2m} ,

moderate T_{2m}) compared to earlier, in June–July, and later, in September (moderate q_{2m} , high T_{2m}).

In contrast, their respective seasonal dynamics leads to enhance the fluctuations of the lifting condensation level (*lcl*) from the edges to the core of the summer (Fig. 7), as *lcl* is very strongly related to RH_{2m} (Betts, 1997), and more so than to either T_{2m} or q_{2m} alone. The *lcl* is a useful indicator of daytime mixed layer height of cloudy boundary layer, being an estimator of cloud base height. Here, between June and August, on average, the altitude of the daytime *lcl*, $z(lcl)$, drops by about 1 km, and the daytime $z(lcl)$ increase is also significantly weaker (around $100 m h^{-1}$ in August against $160 m h^{-1}$ in June, from 9Z to 16Z).

Simple thermodynamic arguments indicate that the nature of a given θ_e value, that can be either wetter/colder or drier/warmer, matters, as it can affect the type and occurrence of moist

⁸ see Frappart et al. (2009) for an overview of the Gourma site rainfall properties.

convective events, and more broadly the mechanisms of coupling between surface and atmospheric processes. For instance, under given environmental conditions (same surface sensible and evaporative fluxes and atmospheric stability), a “moister/colder” θ_e in the low-levels will favour the development of daytime boundary layer cumulus clouds because it acts to lower $z(lcl)$. Conversely, a “drier/warmer” low-level θ_e will prevent the existence of such clouds. Considering now the development of daytime deep convection, a “drier/warmer” low-level θ_e may actually be more favourable when the atmospheric stability is weak (low lapse-rate). This may be the case when the level of free convection is high, as often encountered over continents in semi-arid regions (Takemi, 1999; Findell and Eltahir, 2003; Taylor and Ellis, 2006). Infact, ECMWF analysed profiles above Agoufou indicate a fairly weak morning lapse-rate from about 1 km AGL up to the top of the Saharan air layer during the monsoon, especially in June and September (Fig. 7b), when $z(lcl)$ is the highest (Fig. 7a).

Conversely, seasonal variations in the magnitude of the surface net LW flux likely play a role in the fact that below 600 m, the dry season prominent early morning stable layer extending from the surface up to about 300 m AGL is replaced by a weaker “elevated”⁹ but still stable layer centred about 400 m AGL from late May to early August (Fig. 7b). It is lower then until late September. While seasonal variations of the daily minimum of T_{2m} and DTR are consistent with a weakening of the stable layer, they do not explain the jump of its core. Such a feature likely involves changes in nighttime downward shear-driven turbulent mixing, as can be operated when a nocturnal low-level jet (NLLJ) is present. This is frequently the case all year long above Agoufou according to the analysis, and more broadly at various locations over West Africa according to observations (Lothon et al., 2008). Sounding data at Niamey also point to an upward shift of the NLLJ on the order of 200 m from before to after the establishment of the monsoon flow (but prior to significant rainfall), if one considers wind speeds in a similar range. This is illustrated in Fig. 7c for two fairly windy months in Niamey (2.2E, 13.5), March (dry) and May (moist but not yet rainy)¹⁰. In March, the early night NLLJ develops from a lower altitude and a stronger (weaker) shear below (above) the jet core is maintained until sunrise. This change in the low-level dynamics developing throughout the night goes along with a change in low-level stability which is qualitatively consistent with the analysis. In any case, the radical changes of the early morning virtual potential temperature (θ_v) vertical structure will act to modify the timing of the daytime convective boundary layer growth. While this growth must be much faster once the nocturnal inversion is eroded in March, it may be more progressive in May, and possibly slowed down later in the day by the more stable, elevated and wider layer, which acts as a daytime “convection inhibiting” layer.

If one considers how the diurnal cycle of $\theta_{e_{2m}}$ evolves along the year (Fig. 8, upper curve), it appears that its changes are strongly framed by q_{2m} (Fig. 5, black curves). As long as the atmosphere is dry, typically from November until April, it mirrors the diurnal cycle of temperature; it is maximum in the afternoon around 15 h LST and its amplitude is large, around 15 K. However, as the atmosphere moistens, from May until July, it flattens and the maximum is shifted earlier in the day, between 9 h and 12 h LST (it is the flattest in June with an amplitude of less than 5 K). Only in August, more than two months after the establishment of the low-level monsoon flow, does $\theta_{e_{2m}}$ exhibit a significant afternoon maximum again – it is then in the same range as found over other Tropical continental regions (e.g., Betts and Jakob, 2002).

Thus, in June and July, i.e. outside of the monsoon core, no significant daytime increase of $\theta_{e_{2m}}$ occurs. Again, during the monsoon retreat, in September and October, the daytime maximum of $\theta_{e_{2m}}$ is reached in the morning, because later in the day, the drying (decreases of q_{2m}) dominates over the daytime warming.

This implies that, during the monsoon, apart from its core, the capacity of the convective boundary layer to grow high is critical to the initiation of daytime moist convection. This points to the significance of surface fluxes and atmospheric low levels (in terms of vertical structure together with circulations likely to develop within them, e.g., afternoon mesoscale circulations).

The core of the monsoon season can be seen as a short period of time during which the arguments above become less relevant. Triggering of moist convection (precipitating or not) becomes easier then, within an atmosphere that has shifted from a dryer to a moister type of regime, with a lower height of the lcl (Fig. 7a) and larger $\theta_{e_{2m}}$, especially during afternoon hours¹¹ (Fig. 8, upper curve). Such a transformation goes along with large changes in the magnitude and diurnal cycle of surface net radiation R^{net} (Fig. 8, dotted and lower black curves). During the moist Summer months, from June to September, net radiation does not vary much at night (cf. also Fig. 6). Thus, these changes take place during daytime hours as further quantified by integrating the monthly mean R^{net} with time of the day (starting from 0 J m^{-2} at 0Z, Fig. 8 grey curve). This shows that the early morning minimum, mostly accounting for the LW nighttime cooling from 0Z to 6Z, is about the same in June and August (-13 and -12 J m^{-2} resp.), but the late afternoon daytime maximum is much stronger in August (148 J m^{-2}) than in June (91 J m^{-2}) and the difference (57 J m^{-2}) is maintained within about 1 J m^{-2} until the end of the 24-h period. Daytime maximum R^{net} is also much larger in August (579 W m^{-2}) than in June (357 W m^{-2}) (Fig. 8 lower black curve). Radiative fluxes are analysed in more details below.

Seasonal cycle of the surface radiative budget

The net surface radiative flux, R^{net} , which can be considered as a proxy for the sum of sensible and latent heat fluxes, displays strong seasonal fluctuations as mentioned above and shown more precisely in Fig. 9. They are even stronger than reported by Verhoef (1999) for areas located in Southern Sahel. R^{net} increases progressively from around 20 W m^{-2} (for 10-day mean values) at the coldest of the dry season, until May, when it reaches around 60 W m^{-2} . It further increases, more sharply, during the monsoon, up to 160 W m^{-2} in late August 2003. The following decrease is fast, and lasts until December. This well-defined pattern results from subtle combination of contrasted and sharp seasonal variations of upward and downward longwave and shortwave fluxes, as shown below.

Shortwave fluxes

The seasonal fluctuations of the incoming solar radiation flux at the surface SW^{in} depart significantly from the seasonal cycle of the incoming solar radiation at the top of the atmosphere (TOA) (Fig. 10, upper curve). The latter displays its maximum in May. However, until the second SZA minimum, around mid-August, it does not changes much (it actually decreases by about 5 W m^{-2}), mostly because the late June maximum of solar zenith angle is only about 8° (to be compared to 38° in late December). SW^{in} actually increases from January to early May, but then weakens sharply until mid-June, while PWV and AOT both increase significantly. Later

⁹ i.e., not tied to the surface.

¹⁰ In May at this more Southern location, the monsoon flux is typically more steadily established than at Agoufou, where June would be a closer “climatological analogues”.

¹¹ Note however that the amplitude of the diurnal cycle of $\theta_{e_{2m}}$ in August varies from one year to the next; it is larger for the more rainy monsoon seasons such as 2003 (not shown).

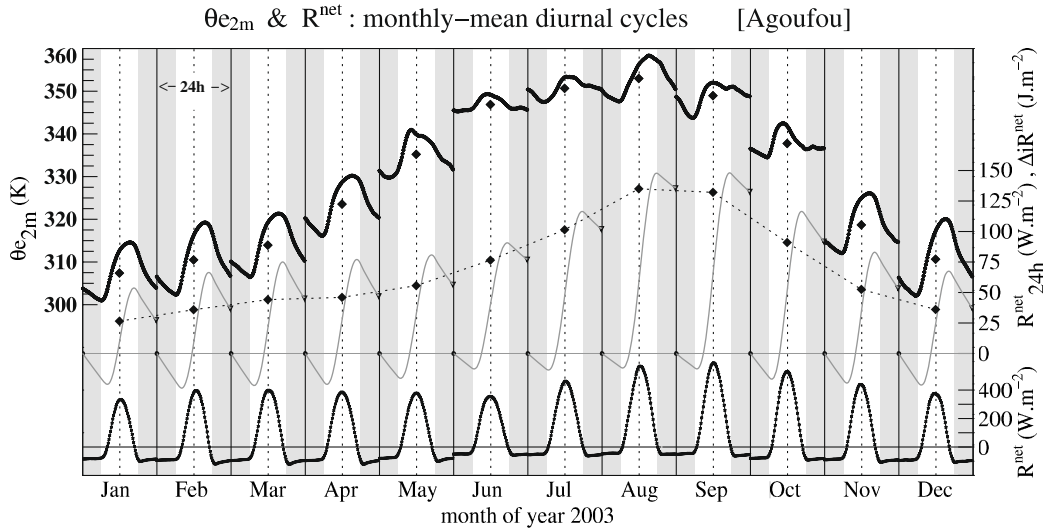


Figure 8. Same as Fig. 5 except for 1-h average $\theta_{e_{2m}}$ (upper curve) and R^{net} (lower curve). The black diamonds and disks are monthly mean values of θ_e and R^{net} . The grey lines stand for monthly means of the integral of R^{net} along 24 h (starting from 0 at 0Z).

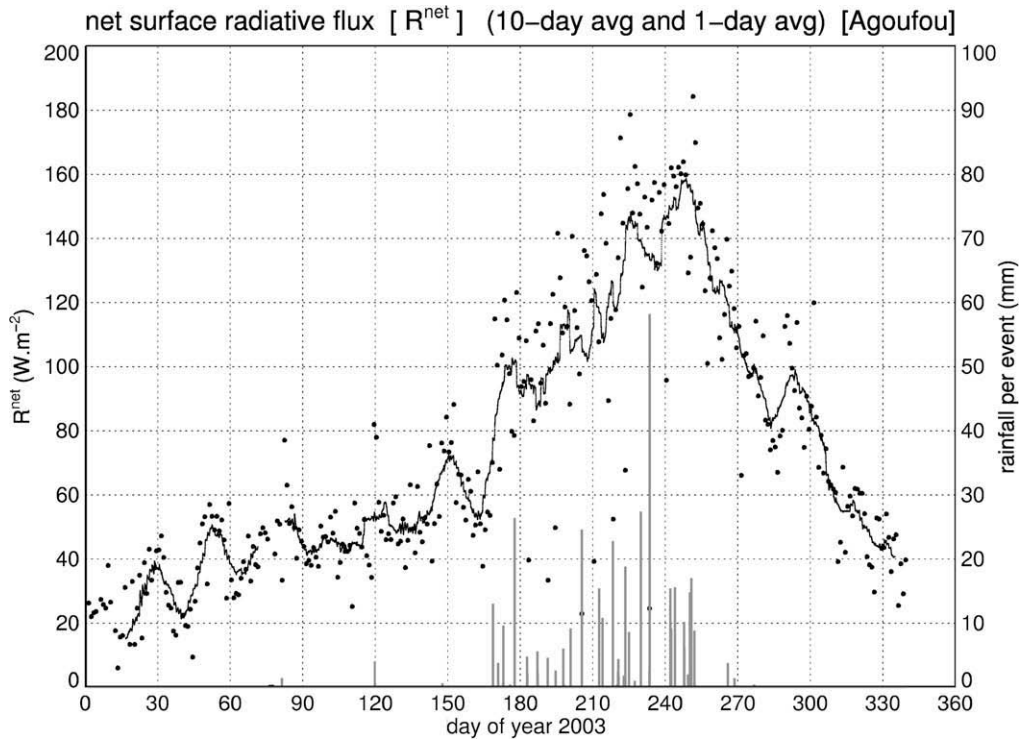


Figure 9. Time series of surface net radiation (R^{net}) and rainfall per event (bottom bars) in 2003, the black line corresponds to a 10-day running mean and the dots to 24-h average values.

on, the seasonal trend is weak, except for a late season SW^{in} decrease from October until December.

The departure of SW^{in} from the solar incoming radiation at the TOA involves the seasonally varying radiative forcing of clouds and aerosols (the seasonal cycle of the AOT varies widely from one year to the next according to the sunphotometer, but AOT is usually higher from Spring until July than later in the year). Occasional thick cloud covers induce sharp drops in 24-h SW^{in} that are not smoothed out by a 10-day average, and account for the few fairly low daily values of R^{net} in July–August (SW^{in} was less than half the clear sky estimate eight times in 2003). Overall, our estimation of clear sky SW^{in} implies a reduction of SW^{in} by clouds and aerosols

of 22–25% for July–August (using criterion $[C_1]$ and respectively $N = 10$ and 30). This corresponds to a SW^{in} reduction of about 70–80 $W m^{-2}$, i.e. a fairly significant magnitude, even if much less than found over more humid Tropical continental areas (e.g., Strong et al., 2005). This result points to the need of an accurate modelling of the daytime cloud field, even for such a semi-arid area; it does not however indicate that the radiative forcing of the clouds is a major actor of the interannual variability of surface radiative fluxes.

On the other hand, the sharp 10-day mean decrease of SW^{in} in May–June, associated with an increase of AOT (Fig. 4), likely involves more directly aerosol and humidity radiative forcing. The

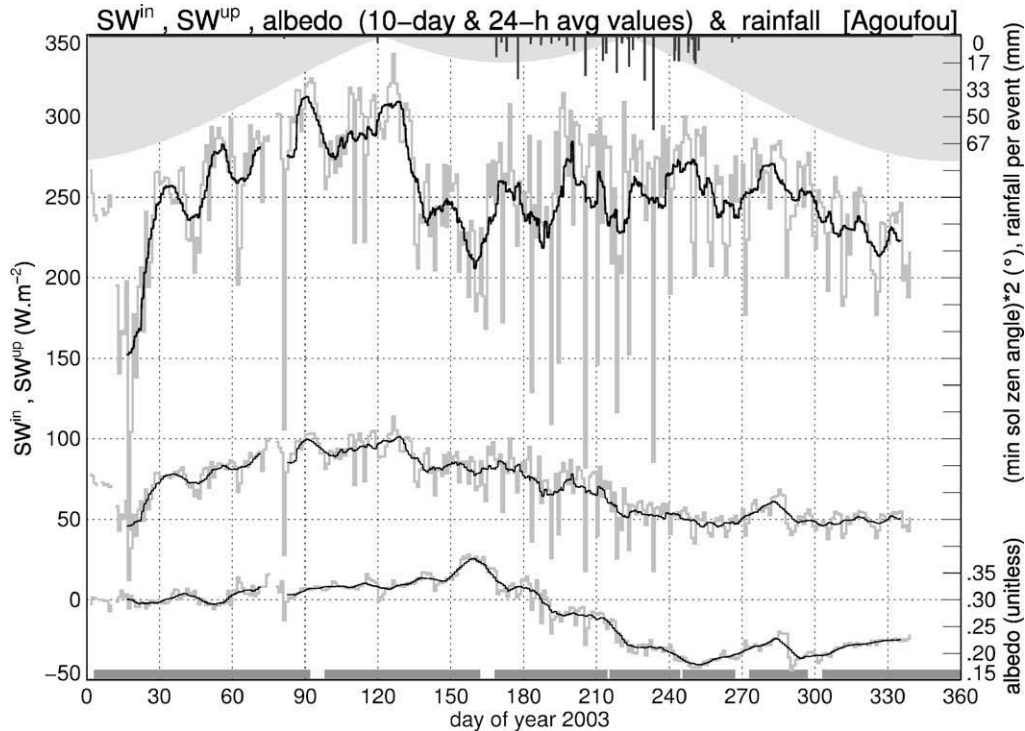


Figure 10. Time series of surface shortwave incoming (SW^{in} , upper curve), outgoing (SW^{up} , middle curve) and albedo (lower curve, right y-axis); the thick black line corresponds to a 10-day running mean and the thin grey line to 24-h average values – upper black bars indicate rainfall events.

relative maximum of SW^{in} around the end of May (day 150) in turn coincides with a local AOT minimum. Apart from isolated maxima, daily AOT is the highest in early June, i.e. several days after the establishment of the monsoon flow, and daily values close to one persist until mid-July, i.e. well after the onset of rainfall.

The solar radiation reflected by the surface, SW^{up} , does not follow the seasonal evolution of SW^{in} (Fig. 10, middle curve). From January until May, its evolution matches relatively closely the SW^{in} increase. However, later on, SW^{up} decreases until September, in sharp contrast with the weak SW^{in} increase. This is due to the seasonal cycle of the surface albedo, a (Fig. 10, lower curve). As shown by Samain et al., 2008, from January until the first rainfall event, the weak increase of a , from 0.3 to about 0.35, is related to the transformation of straw, and to variations of a with spectral wavelength. By the end of August, the albedo is only about 0.2. This trend is not related to a direct effect of soil moisture (Eltahir, 1998). This process actually occurs, and accounts for drops reaching up to 0.1, as also found for other semi-arid areas (Small and Kurc, 2003). It does not last long however. Thus, soil moisture cannot explain the consistent trend developing throughout the monsoon season. This trend is linked to the dynamics of the vegetation cover, which is “darker” than the “bright” sandy surface. The soil wetness affects the albedo in another way however: the repetition of rain events (each accompanied by a short duration drop in albedo) bends the seasonal trend, which induces a systematic lowering of the monsoon season-mean albedo. This effect is enhanced when rainfall events are more numerous. In Agoufou, it is more pronounced early in the season, when the albedo is high and the vegetation cover is low.

Longwave fluxes

The longwave upward flux, LW^{up} (Fig. 11, upper curve) and T_{2m} (Fig. 1) share close seasonal and diurnal evolutions. Indeed, the longwave radiative scaling of DTR proposed by Betts (2006) is sup-

ported by these data (not shown). LW^{up} increases steadily by about 100 W m^{-2} as the surface warms up, from January until mid-May. Its fluctuations are however dominated by a stronger diurnal dynamics, around 200 W m^{-2} .

From mid-May to the end of August, LW^{up} decreases in three steps, each characterized by a distinct diurnal signature. Firstly, LW^{up} decreases, but only slightly and relatively smoothly from the end of May, once the monsoon flux becomes established, until the first significant rainfall event in June. This occurs despite a sharp positive jump of nighttime LW^{up} minima of several tens of W m^{-2} . This is also a period of weaker nocturnal cooling (Fig. 1) and reduced insolation (Fig. 10). In a second step, after the first significant rainfall event of mid-June until the end of July (*early monsoon*), LW^{up} decreases sharply and repeatedly in response to the succession of rainfall events, by several tens of W m^{-2} each time (this induces the series of spikes found in local minima). These values are in the same range as found by Small and Kurc (2003). LW^{up} increases back rapidly after rainfall, but never reaches values as high as prior to the onset of rainfall. Daytime maxima of LW^{up} are much reduced. Finally, LW^{up} reaches its summer lowest in August (*core monsoon*), mostly as a result of a weakening of daytime values. The response to rainfall event is less dramatic than in July because LW^{up} is overall weaker. As SW^{in} is actually slightly higher in August than in July, the enhancement of cloud solar radiative forcing cannot explain this result. In September, after the last rainfall event, LW^{up} increases progressively until the end October, mostly during daytime at first (*retreat*).

The surface downward longwave flux LW^{in} displays a similar range of seasonal fluctuations, but along a distinct trajectory, and its diurnal range is much weaker (Fig. 11, lower curve). LW^{in} is lower during the colder months (down to 180 W m^{-2}), and higher from May to September ($410\text{--}430 \text{ W m}^{-2}$). From January to May and October to December, its synoptic fluctuations closely match those of precipitable water (Fig. 3). From January to April (*dry warming*), they are superimposed to a larger scale positive trend

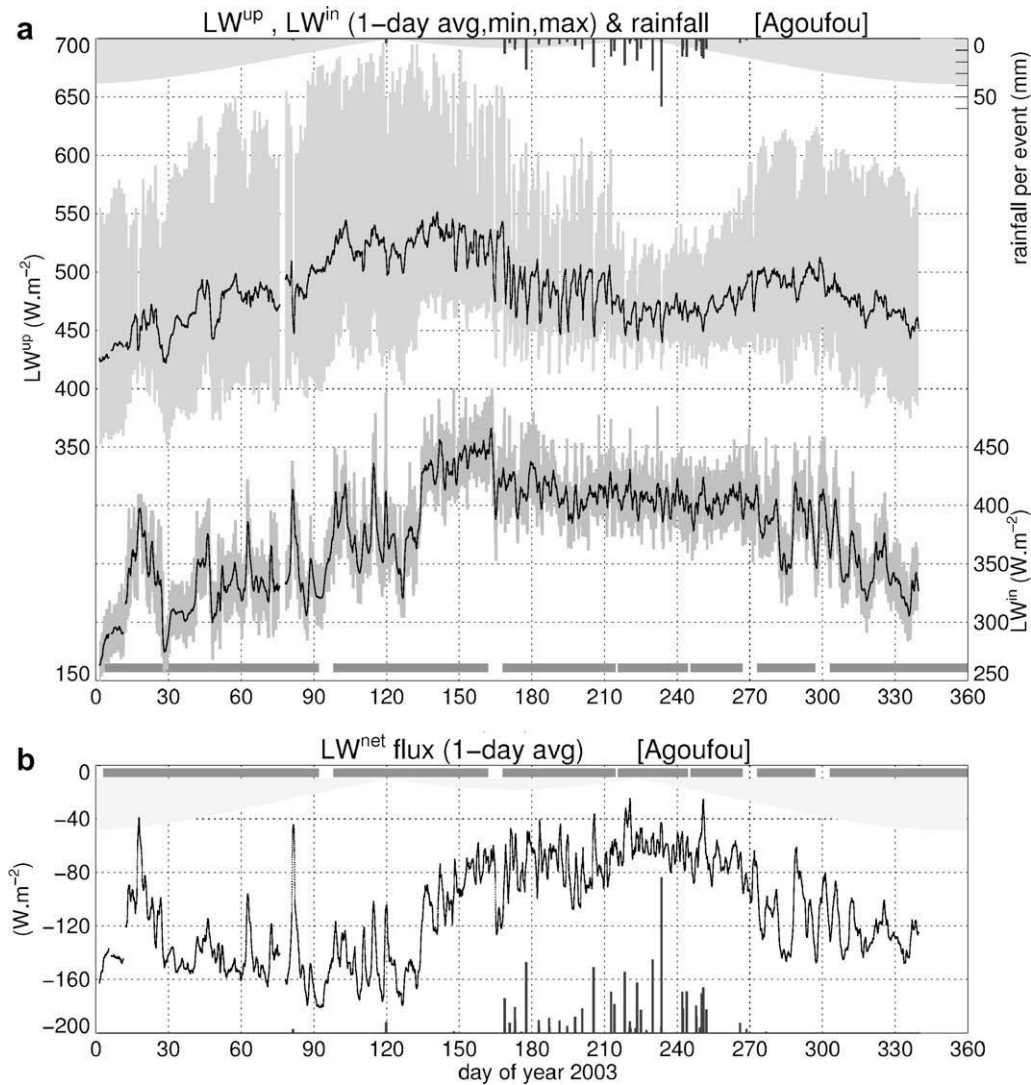


Figure 11. (a) Same as Fig. 1 except for surface longwave fluxes, LW^{up} (upper curve) and LW^{in} (lower curve), (b) 1-day average net longwave flux (LW^{net}).

mirroring the (steeper) trend of LW^{up} , until the sharp jump of LW^{in} initiated at the arrival of the monsoon flow. Thus, LW^{in} is maximum from mid-May to mid-June, i.e. once the monsoon flux is established, but prior to the onset of rainfall, when the atmosphere is quite warm, moist and aerosol-loaded. In fact, from April to Mid-June, LW^{in} fluctuations closely matches those of $-SW^{in}$ (Fig. 10). This feature again is consistent with the observed higher AOT (Fig. 3).

Regarding this moistening period prior to rainfall, it implies: (i) a daytime warming of the optically thicker atmosphere at the expense of the surface, (ii) some partial balance of this daytime process by the nighttime downward radiative emission of this warmer atmosphere (LW^{in} increases), consistent with the higher nighttime surface LW emission and temperature at 2m, but eventually and (iii) from late May until the first rainfall event, a weak decrease of LW^{up} and T_{2m} .

Day-to-day variations of LW^{in} are then markedly weak from mid-June to September. Hence, LW^{in} diurnal variations, on the order of 40 W m^{-2} , appear as relatively large. They are probably linked to the diurnal cycle of surface heating. At sub-diurnal scale, the variations of the cloud cover sometimes induces large LW^{in} fluctuations (e.g. large jumps associated with cloud occurrence), but do not seem to account for the whole day-to-day variability;

in particular, they do not explain the frequent decreases observed the day following a rainfall event. Finally, a weak but persistent negative trend of LW^{in} takes place throughout the monsoon season. It is not explained by PWV evolution (as PWV actually increases from June to August); rather, it likely reflects an overall cooling of the atmosphere as a whole operated by the monsoon phenomenon, and constitutes a way through which LW^{in} damps somehow the increase of R^{net} along the monsoon season.

Surface net radiation and balance of fluxes

The partition of R^{net} into surface longwave and shortwave radiative fluxes (LW^{net} and SW^{net}) shows how the seasonal cycle of R^{net} results from coupled variations of these two fluxes (Fig. 12). From January until the first rainfall event, at first order, LW^{net} and SW^{net} partly cancel each other. This reflects a low capacity of the coupled surface-atmosphere system to efficiently trap the top of the atmosphere increasingly high solar influx, until the atmosphere becomes moist. The balance weakens slightly with time. It is more obvious after May, once the monsoon flow is well established, when both fluxes have significantly changed. However, the increase of LW^{net} in May arises at first because of a sharp jump in atmospheric downwards LW emission which more than

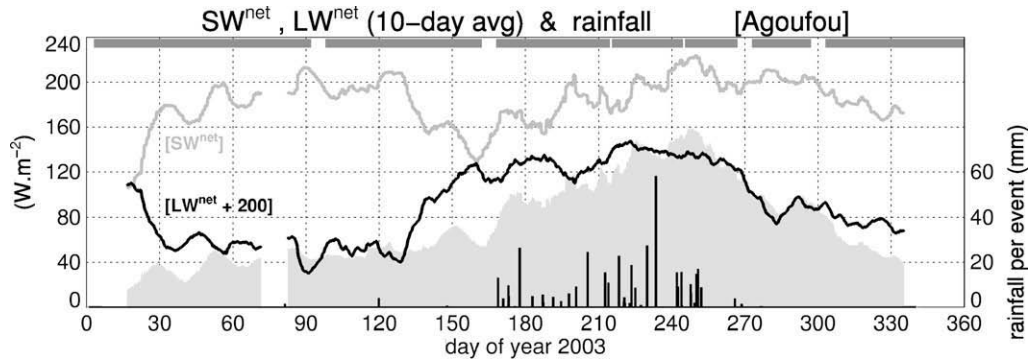


Figure 12. Time series of 10-day mean surface net shortwave flux (SW^{net} , grey line) net longwave flux (LW^{net} , black curve, plotted as $LW^{net} + 200 \text{ W m}^{-2}$), and rainfall per event (black bars); the grey shading corresponds to the surface net radiation (R^{net}).

compensates for the LW^{up} trend, still positive at the surface (for days 125–140). After the first rainfall event and until mid-September, LW^{net} and SW^{net} combined fluctuations eventually lead to a relatively smooth, higher than before, trend of R^{net} that persists throughout the monsoon season. The late monsoon R^{net} trend is however more largely controlled by the progressive increase of SW^{net} , and is linked to albedo changes. Indeed, LW^{net} already started to decrease slowly in August (around day of year 220). As emphasized by Betts (2004) for other regions, LW^{net} is more directly associated to moisture-related variables. In this semi-arid Sahelian location as well, fluctuations of daily-mean LW^{net} and moisture are strongly linked; e.g.; compare daily-mean LW^{net} in Fig. 11b with daily-mean specific humidity q_{2m} , Fig. 1, relative humidity RH_{2m} , Fig. 4, or PWV, Fig. 3.) (Note that this link is not valid for LW^{in} nor LW^{up} when considered separately); This coupling between LW^{net} and moisture is further discussed in next section.

Eventually, a partition of R^{net} into surface incoming and upwelling radiative fluxes (R^{up} and R^{in}) highlights how LW^{in} and SW^{in} seasonal trends largely cancel each other in summer (Fig. 13). As a result, R^{in} remains fairly steady, apart from a weak trend of about $10\text{--}20 \text{ W m}^{-2}$ from mid-April to mid-September, perturbed by fluctuations reaching 30 W m^{-2} on this 10-day mean. The latter are linked to SW^{in} variability, and therefore involve cloud and aerosol radiative forcing (Fig. 14). Thus, the enhancement of R^{net} mostly reflects changes of surface properties that arise in relation with the monsoon, and results from changes of both LW and SW surface upwelling radiative fluxes. LW^{up} is the dominant driver of late Spring and early monsoon R^{net} increase, while the reduction of SW^{up} becomes more significant during the core and late monsoon phases (Fig. 14). Thus, R^{net} can efficiently increase only within

a narrow time window, shifted by about two months with respect to the TOA incoming radiative flux, a window further restricted in time by the retreat of the monsoon flow and fast increase of LW^{up} after the last rain, even though R^{in} does not drop much before mid-October.

Signatures of thermodynamics and radiative fluxes during the monsoon season

The seasonal cycle strongly frames the observed variability, even within the monsoon season, while various coupled modes of fluctuations also emerge at a range of smaller scales, down to the resolution of the dataset. Such relationships are quantified and discussed below, where we adopt a general framework proposed by Betts (2004), applied here to data from the semi-arid central Sahel. Data from six – contrasted – monsoon seasons (2002–2007) are pooled together in order to enhance the size of the sample.

Radiative fluxes

Firstly, Fig. 15a shows that the largest day-to-day variations of the daily-mean incoming radiation R^{in} (around 170 W m^{-2}) are controlled by the incoming solar radiation SW^{in} . It also indicates that heavily cloudy (or aerosol-loaded) conditions are few over the area during daytime hours. No obvious link is found between SW^{in} and LW^{in} variations, in contrast to the strong negative correlation found outside of the monsoon season (not shown). Fig. 15a also indicates that LW^{in} fluctuations are not simply related to the cloud amount and atmospheric water vapour. Indeed, as noted

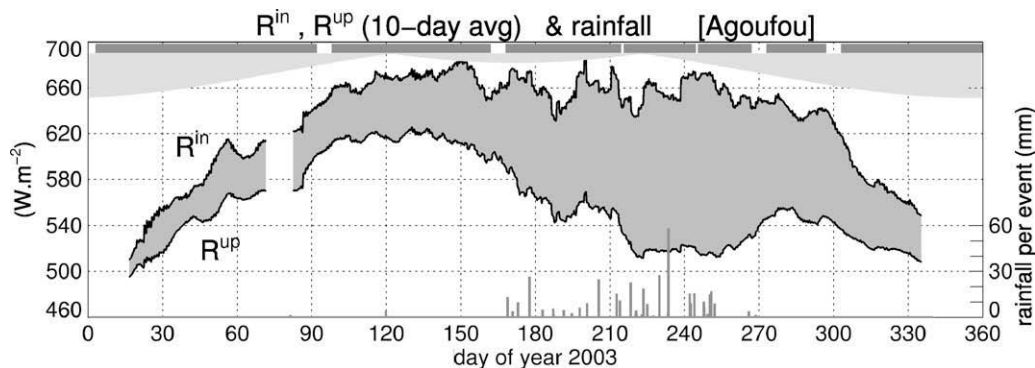


Figure 13. Time series of 10-day mean surface incoming radiative flux ($R^{in} = SW^{in} + LW^{in}$, upper black line) and outgoing radiative ($R^{up} = LW^{up} + SW^{up}$, lower black curve), and rainfall per event (black bars); the vertical thickness of the grey shaded area enclosed within the two black curves gives the magnitude of the surface net radiation (R^{net}) – lower black bars are rainfall per event (right y-axis).

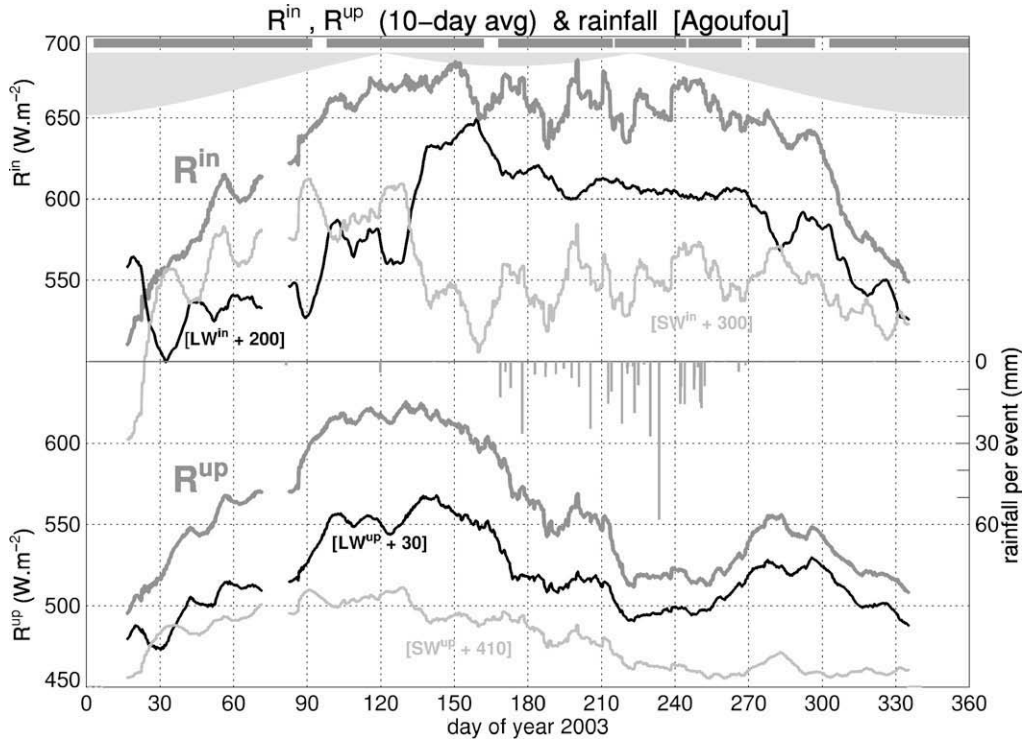


Figure 14. Time series of 10-day mean surface incoming radiative fluxes ($R^{in} = SW^{in} + LW^{in}$, LW^{in} and SW^{in} fluxes, upper curves) outgoing radiative fluxes ($R^{up} = LW^{up} + SW^{up}$, LW^{up} and SW^{up} , lower curves), and rainfall per event (black bars) – lower black bars are rainfall per event (right y-axis). Note that constants have been added to LW and SW incoming and upwelling fluxes in order to make the comparison of their fluctuations easier, their values are provided in the figure.

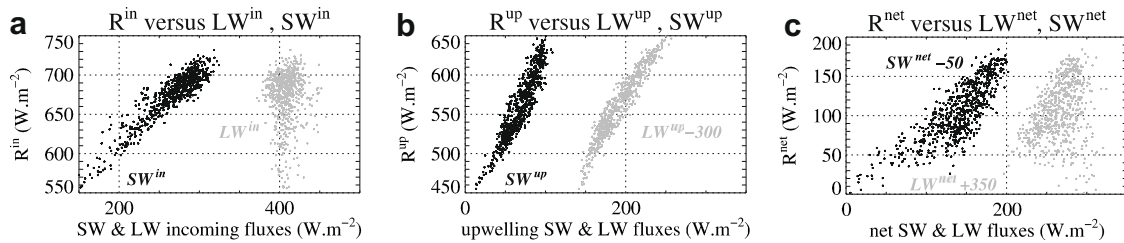


Figure 15. Scatter plots for surface radiative fluxes: (a) incoming radiative flux R^{in} versus its SW and LW components SW^{in} and LW^{in} , (b) as (a) except for upwelling radiative fluxes and (c) R^{net} versus its SW and LW components SW^{net} and LW^{net} – 24-h average values at Agoufou, from June to September of 2002–2007. Note in the figures the values of added constants.

previously, LW^{in} is overall higher in June than in August (Fig. 14, upper black curve), while the sky is less cloudy and precipitable water lower (Fig. 3). Furthermore, the largest difference of monthly mean LW^{in} is actually found during daytime hours (it reaches more than $30 W m^{-2}$ around 14Z to be compared to $15 W m^{-2}$ at 6Z). This points to a significant control of the surface heating on LW^{in} .

Variations of the upward radiative flux R^{up} on the other hand involve both SW^{up} and LW^{up} fluxes (Fig. 15b). R^{up} is more largely driven by LW^{up} fluctuations (grey dots) at higher values of R^{up} (above $550 W m^{-2}$), i.e. outside of August (Fig. 11). It is when the surface thermal emission drops below $550 W m^{-2}$ that the SW^{up} trend becomes relatively more significant. However, the positive correlation between SW^{up} and R^{up} above $R^{up} \sim 550 W m^{-2}$ does not reflect a higher insolation as could be the case if the albedo was constant. Infact, no link is found between SW^{in} and R^{up} (not shown).

Despite a much larger scatter than found in Fig. 15a and b, Fig. 15c shows that the largest day-to-day variations of R^{net} (around $200 W m^{-2}$) are dominantly explained by the range of

fluctuations of SW^{net} . The largest values of SW^{net} are typically reached in August when the albedo is the lowest (Fig. 12). The range of fluctuations of LW^{net} is also quite large (around $120 W m^{-2}$). The scatter in both SW^{net} and LW^{net} is particularly pronounced for values of R^{net} between 50 and $100 W m^{-2}$, as typically found in June (Fig. 9). At that time, day-to-day values of SW^{net} and LW^{net} are more strongly, and negatively, correlated, i.e. to higher SW^{net} often correspond lower LW^{net} . This relationship also holds at lower R^{net} values, below $50 W m^{-2}$, which coincide with rainy and/or daytime-cloudy conditions. However, the increase of R^{net} for values above $70\text{--}80 W m^{-2}$ involves positive trends of both SW^{net} and LW^{net} . An upper limit of LW^{net} , around $-50 W m^{-2}$, also emerges from this diagram (right side of the scatter of grey points). It could be linked to the seasonal dynamics of soil temperature; below the first few tens of cm, soil temperature decreases by a few degrees during the rainy season but remains high (above $30^\circ C$ at 1 m depth) – this contrasts with mid-latitude regions where summer moist convection is related to an increase of soil temperature. This topic needs further investigation.

Thermodynamics

Considering now thermodynamical variables, T_{2m} and q_{2m} follow opposite trends along the monsoon season, as noticed in 3 (see also Fig. 1). Thus, the negative correlation found between them in Fig. 16a is expected. The large scatter implies a significant imprint of synoptic and intraseasonal scales of variability on low-level thermodynamics, beyond their diurnal fluctuations (Fig. 5). This negative correlation holds typically from the arrival to the retreat of the monsoon flow and largely reflects a seasonal scale signature also obvious from 15-min time series (illustrated for JJAS 2003 in Fig. 16g). However, the amplitude of T_{2m} and q_{2m} diurnal cycles and their variations along the summer appear as another factor shaping this “24-h-mean relationship”. Namely, on most days of June and September, and of July to a lesser extend, q_{2m} decreases during daytime hours as T_{2m} increases (as summarized in Fig. 5). This is well captured by monthly composites of their combined daytime (8Z–15Z) evolution (Fig. 16d). Only in August does q_{2m} remain steady (on a daily basis, it increases frequently).

This result is in line with the sharp contrasts in the functioning of the daytime convective BL discussed in Seasonal cycle of meteorological data: thermodynamics and wind. At 2 m AGL, the atmosphere remains rather far from saturation (thick grey line in Fig. 16g). Only during the coolest nights of August or in connection with the passage of convective systems is the couplet (T_{2m}, q_{2m}) constrained by the saturation. In that case however, q_{2m} does not drop below 13–14 g kg^{-1} as the temperature never drops below 20 °C; i.e. q_{2m} remains then significantly higher than in the afternoon of the predominant number of fair weather “drying days”. Furthermore, the departure from saturation implies that evaporation of falling rainfall can be large.

In June prior to the occurrence of rainfall events, when the soil is dry, low-level moisture is mostly supplied by the monsoon flow, as locally, the surface evapotranspiration is low. Thus, R^{net} is more indicative of the magnitude of surface sensible heat flux (Timouk et al., 2009). The actual role played by the infrared flux LW^{up} needs to be explored further but, given its magnitude and the amplitude of the diurnal cycle of LW^{net} (Fig. 6), it should contribute

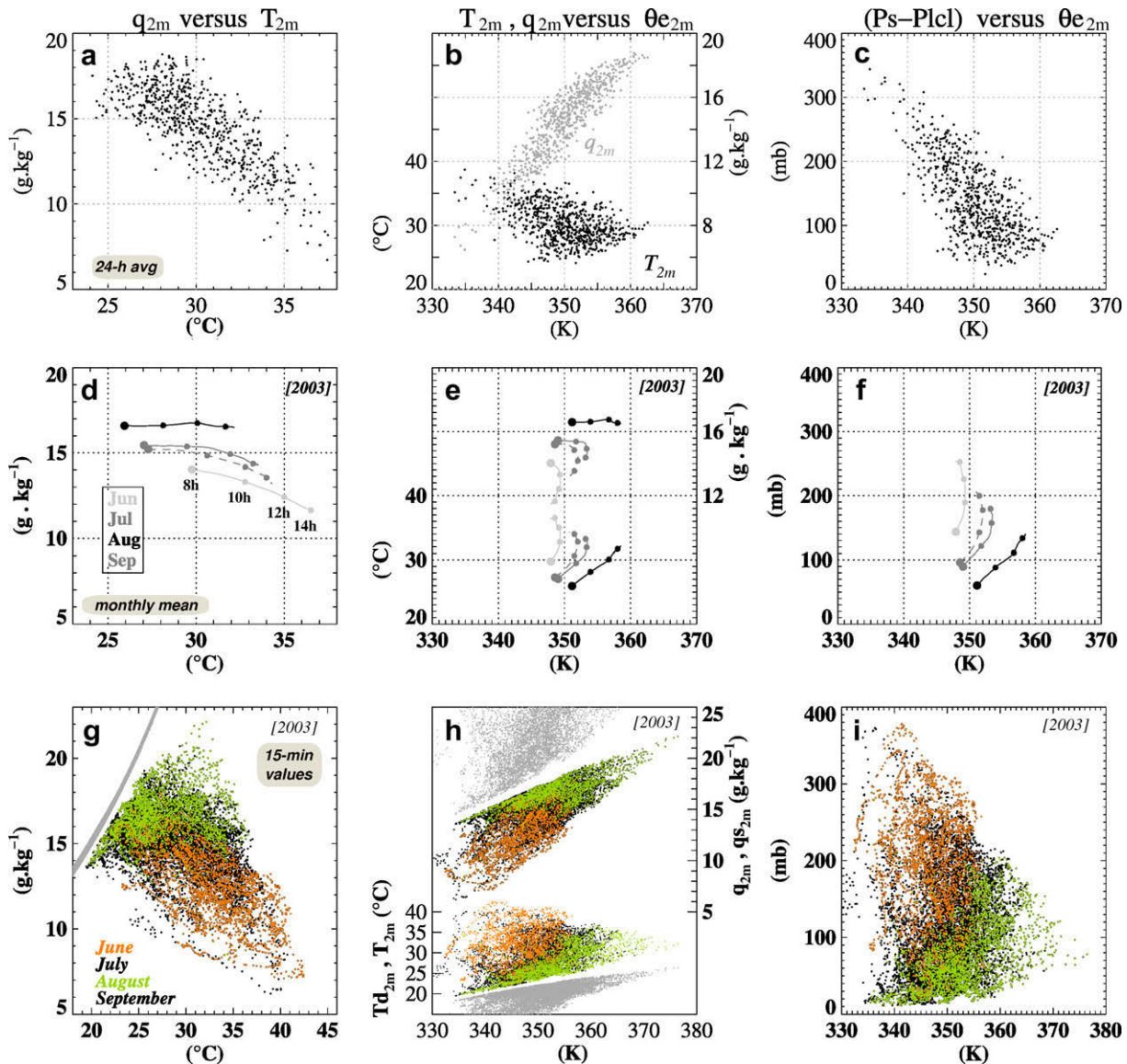


Figure 16. Same as Fig. 15 except for thermodynamic variables: (a) q_{2m} versus T_{2m} , (b) T_{2m} , q_{2m} versus $\theta_{e,2m}$ and (c) $(Ps-Plcl)$ versus $\theta_{e,2m}$; (d), (e) and (f) same as (a), (b) and (c) except for monthly mean daytime variations (8Z–15Z) in June, July, August and September. The thicker disk indicates the value at 8Z, (g), (h) and (i) same as (a), (b) and (c) except for 15-min values, orange and green colours are used for June and August respectively, the upper (lower) grey dots indicate q_{2m} at saturation (dewpoint T_d).

to the daytime heating of the lower levels (e.g., Shi and Smith, 1992). In any case, our results suggest large mixing with upper dryer layers during daytime via processes occurring at the surface and in the low levels; they only decay during the few weeks coinciding with the core of the monsoon season. Such a mechanism, by bringing specific humidity upwards, acts against the low-level moistening associated with the monsoon phenomenon. Because the circulation above is dominated by a strong easterly flow (Fig. 2), once brought high enough, atmospheric water can then be transported away, typically to the West-South-West, thus limiting also the local build-up of upper-level moistening (for a negative gradient of moisture from the WSW to the ENE).

Overall, the monsoon season θe_{2m} increases under moister and colder conditions (Fig. 16b, and Figs. 4 and 1), as a result of the approximately -1 g kg^{-1} per 1 K trend of q_{2m} with T_{2m} (Fig. 16a). Only in August again does this tendency vanish. Then, the higher θe_{2m} values are reached for local maxima of T_{2m} , when q_{2m} is high (Fig. 16h). Therefore, the increase of θe_{2m} is associated with a lowering of the height of the lcl (Fig. 16c). The widening of the spread at high θe values involves distinct changes in the diurnal cycle of both θe and lcl during the Summer (Fig. 16f). These variations reflect the semi-arid character of the region, for which the rainy season involves transitions from hotter-drier to cooler moister atmospheric conditions. They depart from the weaker changes of lcl and lower θe_{2m} observed over mid-latitude lands in Summer (Betts and Ball, 1998). On the other hand, during the less windy monsoon cores of good monsoon years, for a few weeks, lcl and θe_{2m} are very close to values reported for Amazonia (Betts et al. 2002), both in terms of daily mean and diurnal range.

Coupling between surface radiation and thermodynamics

An important feature that this Sahelian site shares with other continental regions is the strong link between lcl and LW^{net} flux shown in Fig. 17a. During the monsoon, when LW^{in} does not fluctuate much (Fig. 11a, lower curve), it emphasizes the strong coupling linking the surface temperature (that can be largely interpreted here as a rainfall induced-cooling) to the mixed layer height (or cloud base). Our results actually extend the range of validity previously documented under fairly distinct climatological conditions (Betts, 2004). The larger scatter at higher lcl values corresponds to days when the atmosphere was more heavily aerosol-loaded, in June (Figs. 3 and 7a). Also specific to this area is the fact that R^{net} increases even more sharply when the lcl is lower (Figs. 9 and 7a), beyond the scatter induced by the few heavily cloudy days, as summarized in Fig. 17b. This involves the rather limited increase of the cloud SW radiative forcing during the monsoon season (e.g.; around 15 W m^{-2} from June to August in 2003) and the overall decrease of surface albedo (Fig. 10, lower curve).

Thus, both θe and R^{net} increase at lower lcl heights (Fig. 16c and Fig. 17b). Eventually, they are found to be positively related (Fig. 17c). It appears that the wider scatter characterizing the lower lcl values corresponds to lower and higher ($R^{net}, \theta e$) couplets as such an asymmetry is not obvious in Fig. 17c.

This result is broadly consistent with previous studies which have related low-level moist static energy to soil moisture through consideration of the surface energy balance (Eltahir, 1998; Schär et al., 1999). In the present case, the strong and fast increase of R^{net} along the monsoon season is mostly explained by the decrease of both surface LW emission and SW reflection, while the increase of θe involves a lowering of mixed layer height (lcl) associated with cooler moister conditions in the low levels.

However, several distinct features are worth summarizing here in view of how the relationship displayed in Fig. 17c is established. Firstly, the surface incoming LW flux does not increase as the atmosphere becomes moister and cloudier; the opposite actually occurs (Fig. 11a lower curve, and Figs. 3 and 4). Secondly, the cloud shortwave radiative impact is found to be significant (several tens of W m^{-2}); nevertheless, from June to August, SW^{in} displays a positive trend (Fig. 10, upper curve), involving a weakening of the aerosol radiative impact. Thirdly, the decrease of SW^{up} involves variations of the albedo from early June to late September (Fig. 10, lower curve) that are more directly related to the fast growth of the vegetation (in response to summer rainfall) than to soil moisture induced darkening of the surface (Samain et al., 2008). Finally, this relationship involves the transition from the edges of the monsoon (lower θe and R^{net}) to its core (higher θe and R^{net}). It seems however that in June (August), R^{net} increases somewhat less (more) in response to θe increase (not shown). This is consistent with θe being more strongly related to the supply of moisture by advection in June, within a drier atmospheric regime than in August, and θe increase being more regulated by moist convective processes during the core of the monsoon. In this respect, it would be useful to carry out studies at smaller time scales; for instance, fluctuations of thermodynamics and surface radiation associated with moist convective events could be documented by composite time series centred on such events and covering time periods of a few days.

Each year, the monsoon season is characterized by a strong temporal dynamics. Its interannual variability involves fluctuations of these parameters. These fluctuations in turn are well framed by the relationships emphasized above. In particular, a more rainy monsoon season is locally associated with overall higher θe and R^{net} (not shown). All these features are broadly consistent with the predominance of a positive feedback loop between soil moisture and convective rainfall, among other feedbacks operating during the monsoon season. Namely, considering the core of the monsoon, when most of the rainfall is falling, this loop would involve the following. A higher R^{net} is dominantly accounted for by

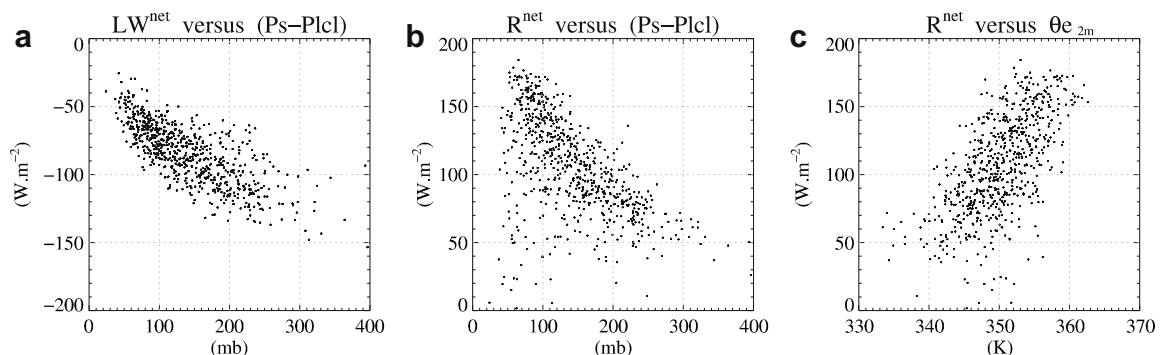


Figure 17. Same as Fig. 15 except for thermodynamic radiative couplets: (a) LW^{net} versus $(Ps-Plcl)$, (b) R^{net} versus $(Ps-Plcl)$ and (c) R^{net} versus θe_{2m} .

a lower LW^{up} . LW^{up} in turn is strongly controlled by rainfall. Thus, a higher R^{net} is also associated with larger soil moisture contents and evaporative fractions. The change in the partition between sensible (H) and latent (LE) heat fluxes acts to increase low-level θe , via an increase of LE and a weakening of the daytime vertical dilution of θe by turbulent mixing (at low H , Timouk et al., 2009). A higher θe in turn helps to overcome convective inhibition and favours further the occurrence of convective rainfall, leading to higher soil moisture contents.

Conclusion

A comprehensive analysis of the seasonal cycle of meteorological and radiative fluxes over the grassland of central Sahel (1.5 W, 15.3 N) has been carried out with surface data, namely in Agoufou, within the Malian Gourma. It comprises an investigation of seasonal changes of their diurnal cycles. Relationships linking radiative and thermodynamic parameters are identified from daily-mean values and monthly mean diurnal cycles.

It is shown that this 6-year long dataset provides a fairly consistent picture of the widely contrasted conditions encountered along the year at this continental semi-arid location. This study emphasizes sharp and coupled modifications of the low-level thermodynamics and surface radiative fluxes, which involve processes of varied nature.

The seasonal cycle of thermodynamic parameters is characterized by a late May maximum of T_{2m} (Fig. 1) followed by an August maximum of θe_{2m} (Fig. 4), taking place, respectively, near the first maximum of incoming solar radiation at the top of the atmosphere and around the second minimum of solar zenith angle, within the core of the rainy monsoon season.

The Spring T_{2m} maximum typically occurs once the monsoon flow becomes more steadily established but prior to the first significant rainfall. It is due to a strong enhancement of nighttime temperature on the order of 5 K, leading to a decrease of the DTR. This coincides with both a significant increase of nighttime surface LW emission and an enhancement of the incoming LW flux of the hot and moist atmosphere (each by a few tens of $W\ m^{-2}$, Fig. 11a). As a result, the net LW loss at the surface (LW^{net}) decreases by several tens of $W\ m^{-2}$ (Fig. 11b). Thus, the surface is less radiatively decoupled from the atmosphere above; consistently, at the surface, nighttime wind speed increases (Fig. 6). This coupled thermal-dynamic weakening of diurnal ranges at 2m is consistent with sounding data at low levels; it involves atmospheric moisture, via its radiative properties, and therefore the monsoon flow in this “radiative” respect as well.

Despite an increasingly high incoming solar flux at the TOA, the positive trend leading to the Spring T_{2m} maximum weakens significantly in April–May (i.e. as the – moist – monsoon flow progressively dominates the atmospheric circulation at low levels), compared to earlier on, from January to March. Similarly, the negative T_{2m} trend following the broad T_{2m} maximum is weak prior to rainfall. This implies that a mechanism is operating at damping temperature fluctuations during this transition period, at time scales of a few days, when Agoufou lies within the Heat Low.

The late summer θe_{2m} maximum on the other hand coincides with the August q_{2m} yearly-maximum, and takes place once the monsoon flow has already weakened (Fig. 2). The seasonal course of θe_{2m} is not explained by q_{2m} alone however. From early May until late June, θe_{2m} is higher by 5–10 K than it would have been if temperatures had been those of August. More broadly, the opposite T_{2m} and q_{2m} seasonal fluctuations lead to some damping of θe_{2m} fluctuations along the summer, and to a sharpening of the θe_{2m} jump in the early monsoon season (Figs. 4 and 1). Opposite diurnal fluctuations of T_{2m} and q_{2m} also shape a relatively flat diurnal cycle of θe_{2m} (Fig. 8, upper curve), apart from a limited time period, with-

in the core of the monsoon season in August, when q_{2m} stops decreasing during daytime (Fig. 5). The relatively high values of θe_{2m} encountered in the early monsoon season occur as the atmospheric lapse-rate is still fairly weak. It is suggested that this feature helps the development of moist convection within a still relatively moisture-limited environment.

Surface radiative data show that R^{net} increases dramatically from around $20\ W\ m^{-2}$ (for 10-day mean values) at the coldest of the dry season to $120\text{--}160\ W\ m^{-2}$ at the end of August in Agoufou (Fig. 9). The increase is not regular, but sharper during the monsoon than before, and the decrease faster than previous increases. The seasonal cycle of R^{net} arises from very distinct shortwave and longwave fluctuations (Fig. 12) that are both strongly shaped along the monsoon season by transformation of surface properties related to rainfall events and vegetation phenology, leading to a reduction of the upwelling longwave and shortwave fluxes (Figs. 13 and 14); these effects take place at different scales.

During the monsoon, clouds and aerosols reduce the incoming solar radiation by about 25% ($70\ W\ m^{-2}$). They also significantly enhance the day-to-day variability of R^{net} . However, the Summer increase of R^{net} is not related to any significant trend of the incoming radiative flux: LW^{in} displays a weak negative trend that balances somehow an overall positive trend of SW^{in} (the latter arises despite an enhancement of cloud radiative forcing from June to August, possibly linked to the decrease of AOT and changes in clear sky SW absorption).

When compared to other continental regions, these results emphasize some important common features, but also contrasted modes of functioning of this Sahelian site. Thus, strong links are found between moisture and LW^{net} , and they are quantitatively consistent with previous studies. Namely, lower heights of the lcl (a proxy for cloud base and mixed layer height) are associated with higher surface LW^{net} (Fig. 17a). However, a lower lcl is also associated with higher R^{net} (Fig. 17b). This feature is linked to the semi-arid nature of the local climate, where reduction of the incoming solar radiation by the cloud cover is weaker than other sources of variations of R^{net} . The strong seasonal dynamics associated with the transition from a dry hot Spring to a cooler moist Summer climate also involves large transformations of the diurnal cycle, even within the monsoon season, which significantly affect both thermodynamical, dynamical and radiative fields (and low-level dynamics). Thus, the positive correlation identified here between R^{net} and θe_{2m} (Fig. 17c) results from a complex interplay among processes.

It is therefore not surprising that modelling such links in a quantitative way is currently difficult. The observational results presented in this study provide valuable ground truth for advancing on this issue. It will be useful to derive such diagnostics from models as they characterize basic aspects of the energetics of surface–atmosphere coupling in a synthetic way.

Acknowledgments

We are grateful to Hamma Maïga for his involvement in the installation and maintenance of the Agoufou AWS. We also thank P. Goloub and collaborators for establishing and maintaining the Agoufou sunphotometer AERONET site. The ECMWF analysis was retrieved from the MARS archive. The sounding data were acquired as part of the AMMA radiosonde program, coordinated by D. Parker and A. Fink, and operated by the *agence pour la sécurité de la navigation aérienne en Afrique et à Madagascar* (ASECNA). Based on a French initiative, AMMA has been established by an international group and is currently funded by a large number of agencies, especially from France, the UK, and Africa. It has been the beneficiary of a major financial contribution from the European Community's Sixth Framework Research Programme. Detailed information on

scientific coordination and funding is available on the AMMA international web site (<http://www.amma-eu.org/>). Eventually, we thank F. Couvreur for several discussions, A.K. Betts for his valuable comments on a previous version of this manuscript, and the two reviewers.

References

- Ag Mahmoud, M., 1992. In: Le Floch, R. (Ed.), *Le haut Gourma Central*, second ed. CEFE/CNRS, Montpellier, pp. 133.
- Agrhymet, 2003. September 2003 monthly bulletin, permanent interstate committee for drought control in the Sahel, M 06/03. <<http://www.agrhymet.ne/bulletin-mensuel.htm>>.
- Betts, A.K., 1997. The parameterization of deep convection. In: Smith, R.K. (Ed.), *The Physics and Parameterization of Moist Atmospheric Convection*, NATO ASI Ser. C, vol. 505. Kluwer Acad., Norwell, MA, pp. 255–279. 498 pp.
- Betts, A.K., Ball, J.H., 1998. FIFE surface climate and site-average dataset 1987–89. *J. Atmos. Sci.* 55, 1091–1108.
- Betts, A.K., Fuentes, J.D., Garstang, M., Ball, J.H., 2002. Surface diurnal cycle and boundary layer structure over Rondônia during the rainy season. *J. Geophys. Res.* 107 (20), 8065.
- Betts, A.K., 2004. Understanding hydrometeorology using global models. *Bull. Amer. Meteor. Soc.* 85, 1673–1688.
- Betts, A.K., 2006. Radiative scaling of the nocturnal boundary layer and the diurnal temperature range. *J. Geophys. Res.* 111, D07105. doi:10.1029/2005JD006560.
- Bock, O., Bouin, M.N., Doerflinger, E., Collard, P., Masson, F., Meynadier, R., Nahmani, S., Koité, M., Gaptia Lawan Balawan, K., Didé, F., Ouedraogo, D., Pokperlaar, S., Ngamini, J.-B., Lafore, J.P., Janicot, S., Guichard, F., Nuret, M., 2008. The West African Monsoon observed with ground-based GPS receivers during AMMA. *J. Geophys. Res.* 113, D21105. doi:10.1029/2008JD010327.
- Charney, J.G., 1975. Dynamics of deserts and drought in the Sahel. *Quart. J. Roy. Meteor. Soc.* 101, 193–202.
- Dirmeyer, P.A., Koster, R.D., Guo, Z., 2007. Do global models properly represent the feedback between land and atmosphere? *J. Hydromet.* 7, 1177–1198.
- Eltahir, E.A.B., 1998. A soil moisture–rainfall feedback mechanism, 1, Theory and observations. *Water Resour. Res.* 34, 765–776.
- Eltahir, E.A.B.C., Gong, C., 1996. Dynamics of wet and dry years in West Africa. *J. Climate* 9 (5), 1030–1042.
- Findell, K.L., Eltahir, E.A.B., 2003. Atmospheric controls on soil moisture–boundary layer interactions. Part II: feedbacks within the continental United States. *J. Hydromet.* 4, 570–583.
- Frappart, F., Hiernaux, P., Guichard, F., Mougou, E., Kergoat, L., Arjounin, M., Lavenu, F., Koité, M., Paturol, J.-E., Lebel, T., 2009. Rainfall regime over the Sahelian climate gradient in the Gourma, Mali. *J. Hydrol.* 375 (1–2), 128–142.
- Guichard, F., Couvreur, F., Nuret, M., Agusti-Panareda, A., 2008. Roles of low-level thermodynamics on surface–convection interactions over West-Africa. European Geosciences Union General Assembly 2008, Vienna, Austria, 13–18 April, 2008.
- Goutorbe, J.P. et al., 1994. HAPEX-Sahel - a large-scale study of land–atmosphere interactions in the semi-arid tropics. *Ann. Geophys.* 12, 53–64.
- Lothon, M., Saïd, F., Lohou, F., Campistron, B., 2008. Observation of the diurnal cycle in the low troposphere of West Africa Mon.. *Weather. Rev.* 136, 3477–3500.
- Nicholson, S., 2000. Land surface processes and Sahel climate. *Rev. Geophys.* 38, 117–139.
- Nuret, M., Lafore, J.P., Bock, O., Guichard, F., Agusti-Panareda, A., N'Gamini, J.-B., Redelsperger, J.-L., 2008. Correction of humidity bias for Vaisala RS80 sondes during AMMA 2006 Observing Period. *J. Atmos. Ocean Tech.* 25, 2152–2158.
- Parker, D.J., Burton, R.R., Diongue-Niang, A., Ellis, R.J., Felton, M., Taylor, C.M., Thorncroft, C.D., Bessemoulin, P., Tompkins, A.M., 2005. The diurnal cycle of the West African monsoon circulation. *Quart. J. Roy. Meteor. Soc.* 131, 2839–2860.
- Parker, D.J., Fink, A., Janicot, S., Ngamini, J.-B., Douglas, M., Afesimama, E., Agusti-Panareda, A., Beljaars, A., Dide, F., Diedhiou, A., Lebel, T., Polcher, J., Redelsperger, J.-L., Thorncroft, C., Wilson, G.A., 2008. The AMMA radiosonde program and its implications for the future of atmospheric monitoring over Africa. *Bull. Amer. Meteor. Soc.* 89, 1015–1027.
- Ramel, R., Galle, H., Messenger, C., 2006. On the northward shift of the West African monsoon. *Climate Dyn.* 26, 429–440.
- Redelsperger, J.-L., Parsons, D., Guichard, F., 2002. Recovery processes and factors limiting cloud top height following the arrival of a dry intrusion observed during TOGA-COARE. *J. Atmos. Sci.* 59, 2438–2457.
- Redelsperger, J.-L., Thorncroft, C., Diedhiou, A., Lebel, T., Parker, D.J., Polcher, J., 2006. African Monsoon Multidisciplinary Analysis (AMMA): An international research project and field campaign. *Bull. Amer. Meteor. Soc.* 87, 1739–1746.
- Samain, O., Kergoat, L., Hiernaux, P., Guichard, F., Mougou, E., Timouk, F., Lavenu, F., 2008. Analysis of the in situ and MODIS albedo variability at multiple time scales in the Sahel. *J. Geophys. Res.* 113, D14119. doi:10.1029/2007JD009174.
- Schär, C., Lüthi, D., Beyerle, U., Heise, E., 1999. The soil–precipitation feedback: a process study with a regional climate model. *J. Climate* 12, 722–741.
- Shi, L., Smith, E.A., 1992. Surface forcing of the infrared cooling profile over the Tibetan plateau. Part II: cooling-rate variation over large-scale plateau domain during Summer monsoon transition. *J. Atmos. Sci.* 49, 823–844.
- Small, E., Kurc, S., 2003. Tight coupling between soil moisture and the surface radiation budget in semiarid environments: implications for land–atmosphere interactions. *Water Resour. Res.* 39 (10), 1278. doi:10.1029/2002WR001297.
- Strong, C., Fuentes, J.D., Garstang, M., Betts, A.K., 2005. Daytime cycle of low-level clouds and the tropical convective boundary layer in Southwestern Amazonia. *J. Appl. Meteor.* 44, 1607–1619.
- Takemi, T., 1999. Structure and evolution of a severe squall line over the arid region in Northwest China. *Mon. Weather Rev.* 127, 1301–1309.
- Taylor, C.M., Ellis, R.J., 2006. Satellite detection of soil moisture impacts on convection at the mesoscale. *Geophys. Res. Lett.* 33, L03404.
- Taylor, C.M., Lebel, T., 1998. Observational evidence of persistent convective-scale rainfall patterns. *Mon. Weather Rev.* 126, 1597–1607.
- Timouk, F., Kergoat, L., Mougou, E., Lloyd, C., Ceschia, E., De Rosnay, P., Hiernaux, P., Demarez, V., 2009. Response of sensible heat flux to water regime and vegetation development in a central Sahelian landscape. *J. Hydrol.* 375 (1–2), 178–189.
- Verhoef, A., 1999. Seasonal variation of surface energy balance over two Sahelian surface. *Int. J. Climatol.* 19, 1267–1277.
- Xue, Y., 1997. Biosphere feedback on regional climate in tropical North Africa. *Quart. J. Roy. Meteor. Soc.* 123, 1483–1515.
- Zheng, X., Eltahir, E.A.B., 1998. A soil moisture–rainfall feedback mechanism, 2, Numerical experiments. *Water Resour. Res.* 34, 777–785.